

Imaging VGOS observations and investigating source structure effects

Ming H Xu¹, Tuomas Savolainen¹, Nataliya Zubko², Markku Poutanen³, Susanne Lunz⁴, Harald Schuh⁵, and Guangli Wang⁶

¹Aalto University

²Finnish Geospatial Research Institute

³Finnish Geodetic Institute

⁴GFZ German Research Centre for Geosciences

⁵GFZ

⁶Shanghai Astronomical Observatory (CAS)

November 22, 2022

Abstract

The next-generation, broadband geodetic very-long-baseline interferometry system, named VGOS, is being developed globally with an aim to achieve 1 mm accuracy for station positions. Currently, the systematic errors in VGOS observations are still about one order-of-magnitude larger than this aim. In this study, we demonstrate that it is feasible to make images directly from VGOS observations without the need of complicated calibrations and determine the source structure effects in VGOS broadband delays through the process of model fitting to the structure phases from our imaging results. Source structure effects are investigated in detail, and it is shown that the systematic errors in VGOS observations are well explained by these effects. For instance, the root-mean-square (RMS) closure delays of the observations of sources 0016+731 and 1030+415 are 24.9 ps and 50.2 ps in session VO0034, respectively; by correcting source structure effects based on the images, the RMS values of the residual closure delays are 5.5 ps and 10.1 ps. The jumps in delay observables with magnitudes of several hundreds of picoseconds are found to be caused by 2π phase shifts among the four bands due to strong source structure effects. The impact of the alignment of the images at the four frequency bands in VGOS is discussed. Our study provides a methodology of deriving images of radio sources at the four bands of VGOS observations and discusses the alignment of the four-band images, which is fundamental to mitigate systematic effects.

Imaging VGOS observations and investigating source structure effects

Ming H. Xu^{1,2,6,7}, Tuomas Savolainen^{1,2,3}, Nataliya Zubko⁴, Markku Poutanen⁴, Susanne Lunz⁵, Harald Schuh^{6,5}, Guang L. Wang⁷

¹Aalto University Metsähovi Radio Observatory, Metsähovintie 114, 02540 Kylmälä, Finland

²Aalto University Department of Electronics and Nanoengineering, PL15500, FI-00076 Aalto, Finland

³Max-Planck-Institut für Radioastronomie, Auf dem Hügel 69, 53121 Bonn, Germany

⁴Finnish Geospatial Research Institute, Geodeetinrinne 2, FIN-02430 Masala, Finland

⁵DeutschesGeoForschungsZentrum (GFZ), Potsdam, Telegrafenberg, 14473 Potsdam, Germany

⁶Institute of Geodesy and Geoinformation Science, Technische Universität Berlin, Straße des 17. Juni 135, 10623, Berlin, Germany

⁷Shanghai Astronomical Observatory, Chinese Academy of Sciences, No. 80 Nandan Road, 200030, Shanghai, P. R. China

Key Points:

- Images of radio sources at the four bands were derived directly from VGOS broadband observations.
- Source structure effects in VGOS observations were modeled and verified.
- The alignments of the images at the various frequency bands were revealed to be very important in correcting source structure effects in VGOS observations.

Abstract

The next-generation, broadband geodetic very-long-baseline interferometry system, named VGOS, is being developed globally with an aim to achieve 1 mm accuracy for station positions. Currently, the systematic errors in VGOS observations are still about one order-of-magnitude larger than this aim. In this study, we demonstrate that it is feasible to make images directly from VGOS observations without the need of complicated calibrations and determine the source structure effects in VGOS broadband delays through the process of model fitting to the structure phases from our imaging results. Source structure effects are investigated in detail, and it is shown that the systematic errors in VGOS observations are well explained by these effects. For instance, the root-mean-square (RMS) closure delays of the observations of sources 0016+731 and 1030+415 are 24.9 ps and 50.2 ps in session VO0034, respectively; by correcting source structure effects based on the images, the RMS values of the residual closure delays are 5.5 ps and 10.1 ps. The jumps in delay observables with magnitudes of several hundreds of picoseconds are found to be caused by 2π phase shifts among the four bands due to strong source structure effects. The impact of the alignment of the images at the four frequency bands in VGOS is discussed. Our study provides a methodology of deriving images of radio sources at the four bands of VGOS observations and discusses the alignment of the four-band images, which is fundamental to mitigate systematic effects.

1 Introduction

Geodetic very-long-baseline interferometry (VLBI) is a space-geodetic technique that has regularly made global astrometric/geodetic observations since 1979, which are the basis for creating the International Celestial Reference Frame (ICRF2; Fey et al., 2015) and obtaining a full set of Earth Orientation Parameters. Together with other three space geodetic techniques, i.e., Global Navigation Satellite Systems (GNSS), Satellite Laser Ranging (SLR) and Doppler Orbitography and Radiopositioning Integrated by Satellite (DORIS), VLBI plays an important role in establishing the International Terrestrial Reference Frame (ITRF; Altamimi et al., 2016). Requirements for the ITRF have increased dramatically since the 1980s, and the most stringent one from sea level studies is 1 mm position accuracy and 0.1 mm/yr velocity stability on global scales.

The International VLBI Service for Geodesy and Astrometry (IVS; Schuh & Behrend, 2012; Nothnagel et al., 2017, please also refer to the IVS website¹) is developing the next-generation geodetic VLBI system, known as the VLBI Global Observing System (VGOS; Niell et al., 2007; Petrachenko et al., 2009) in order to achieve the goal of 1 mm accuracy. This is one order of magnitude beyond the capability of the traditional S/X VLBI system. Although the VGOS observations from the 500-km-long baseline, GGA012M–WESTFORD, have obtained geodetic results of a weighted root-mean-square deviation of the baseline length residuals about the weighted mean of 1.6 mm (Niell et al., 2018), few studies have analyzed error sources in the VGOS observations, for instance source structure effects, to evaluate the capability of this new VLBI system. Source structure effects hardly have any influence on this short baseline but can cause significant errors in observations of longer baselines, as demonstrated by the residual delays from geodetic solutions of VGOS observations in Bolotin et al. (2019). Celestial radio sources observed by geodetic VLBI, mostly quasars, are treated as point-like sources in routine geodetic solutions, but in fact they are resolved on intercontinental baselines. The questions are how large is their effect on the reference frames and how these effects can be corrected or/and mitigated.

The dominant remaining error source in traditional S/X observations was shown to be source structure effects based on analyzing closure delays (Xu et al., 2016, 2017; Anderson &

¹ <https://ivscc.gsfc.nasa.gov/index.html>

Xu, 2018). The study of twenty-one VGOS sessions revealed that the random measurement noise of VGOS group delays was about two picoseconds (ps), while the contributions from systematic error sources were at the level of 20 ps (Xu et al., 2020). Discrete jumps in VGOS delays with magnitudes of several hundreds of picoseconds or even larger have been reported. These systematic error sources were considered to be related to source structure effects, the in-depth investigation of which would require images of radio sources—the brightness distribution over the sky—at the wide frequency range of VGOS observations. It is not possible for the VGOS to achieve its goal without taking source structure effects into account, since they are so overwhelming in VGOS observations even for the sources with minimum structure (Xu et al., 2020). In this paper we attempt to investigate these systematic errors by making images directly from VGOS observations and modeling structure effects from the imaging results.

The paper is structured as follows. In section 2, we introduce the data and the imaging process, perform imaging simulations and determine structure effects in broadband observations. In section 3, we describe the comparison of modeled structure effects and the systematic effects in observations and study the impact of source structure effects. The discussion of the reference points of the images and the so-called core shift effect is presented in section 4 and conclusions are made in section 5.

2 Data and Methodology

2.1 VGOS observations

VGOS observations mainly rely on the advantages from the small (~ 12 meters in diameter) and fast slewing radio telescopes, ultra-wideband receivers (from 2 to 14 GHz), and the expectation of continuous operation, 24 hours a day and seven days a week. They were made simultaneously at four 512-MHz bands centered at 3.3, 5.5, 6.6, and 10.5 GHz with 32 recording channels² (8 channels per band; see the detailed technical description of the observing frequency setup in Niell et al. (2018)). Group delay and differential total electron content (δ TEC) in the line of sight through the ionosphere are estimated simultaneously in the VGOS data processing (Cappallo, 2014). The reported formal errors of group delay observables in databases are just a few picoseconds (ps), and those for δ TEC observables are at the level smaller than 0.1 TECU³. Based on closure analysis in Xu et al. (2020), the structure-induced effect in a group delay observable can be statistically determined from the available closure delays involving that delay observable. It was found that the random measurement noise level of VGOS group delays was 2 ps by combining the observations from the VGOS radio sources that have log closure amplitude root-mean-square values smaller than 0.25 (Xu et al., 2019), and the contributions from other systematic error sources were at the level of 20 ps.

There are 34 IVS VGOS sessions publicly available as of June 2020. However, the study reported here concentrates on two sessions, VT9217⁴ and VO0034⁵, to investigate source structure effects in VGOS in detail and to discuss the difficulties in this process in a concrete manner. A complete investigation on correcting source structure effects in geodetic VLBI solutions for all the VGOS observations available is in preparation. Session VO0034 is the

² On rare occasions there are 31 channels recorded. For instance, in session VO0034 station ONSA13SW recorded with 31 channels with one missing at the highest frequency band. However, we will always refer to as 32 channels in the paper for simplicity.

³ 1 TECU $\equiv 10^{16}$ electrons per square meter.

⁴ It was observed on August 05, 2019. The data are available at <ftp://ivs.bkg.bund.de/pub/vlbi/ivsdata/vgosdb/2019/19AUG05VG.tgz>

⁵ It was observed on February 03, 2020. The data are available at <ftp://ivs.bkg.bund.de/pub/vlbi/ivsdata/vgosdb/2020/20FEB03VG.tgz>

one observed with the most stations among these 34 sessions, and thus has the best (u, v) coverage critical for imaging. Session VT9217 was selected without preference.

VGOS observations in the vgosDB format⁶ based on the NetCDF library⁷ were used to generate the corresponding uvfits data. The correlated amplitudes at the 32 channels, written in the NetCDF file `ChannelInfo_bX.nc` with a variable name of “ChanAmpPhase”, were averaged at each of the four bands to assign the amplitude observables, and the standard deviations were used as their uncertainties. Apparently, the structure differences across the 512 MHz bandwidth of each four bands were ignored in the study⁸. Based on the uncertainties, the signal-to-noise ratios (SNR) were determined. Through careful investigations of phase observables in the vgosDB dataset, it is evident that the phases at the 32 channels stored in the same file with the same variable name as channel amplitude observables are actually residual phases after model fitting rather than the total phases that we needed. Therefore, three types of VGOS observables, namely residual phases, geocentric group delays⁹ and δTEC estimates, were combined together to recover the observed total phases at each of the four bands. The uncertainties of these phase observables were based on the previously derived SNRs from observed amplitudes.

In the VGOS data processing¹⁰, all the four correlation products from the horizontal and vertical polarizations are combined to give a single pseudo-Stokes I observable with an attempt to account for the differential parallactic angles between stations (Cappallo, 2016). Pseudo Stokes I , however, does not take the gain differences between various polarizations or leakage into account. This leads to systematic, non-closing errors in the resulting closure quantities, which depend on the polarizations of radio sources, feed purity, and gain differences between the horizontal and vertical polarizations in a complex manner. So far we ignore these issues and assign the amplitudes and phases as Stokes I coefficients.

For completeness, we give the basic equations that were used to generate the imaging data. Amplitude V at each of the four bands is given as the mean values of channel amplitudes as follows

$$V = \frac{\sum_{i=1}^L V_i}{L}, \quad (1)$$

where V_i is the visibility amplitude in the i -th channel of the band and L is the number of validated channels with a maximum value of 8. Phase ϕ at the band with the central frequency of $\bar{\nu}$ is given by a function of the mean values of the channel residual phases and the group delay and δTEC observables in the observation as follows

$$\phi = \frac{\sum_{i=1}^L \Delta\phi_i}{L} + \tau(\bar{\nu} - \nu_0) - \frac{k \delta\text{TEC}}{\bar{\nu}}, \quad (2)$$

where $\Delta\phi_i$ is the residual phase in the i -th channel of the band, τ and δTEC are the broadband delay and the differential total electron content from the observation, ν_0 is the reference frequency of 6.0 GHz, and k is a constant. $k=1.3445$ when phases are in units of a turn of a cycle, delays in units of nanosecond, frequencies in units of GHz and δTEC in units of TECU

It is impossible to derive accurate SNR for these amplitude and phase observables so far, because (1) most of these VGOS sessions miss the system equivalent flux density mea-

⁶ http://ivscc.bkg.bund.de/publications/gm2016/046_bolotin.etal.pdf

⁷ <https://www.unidata.ucar.edu/software/netcdf/>

⁸ Indeed, this assumption may not hold for some sources. In such cases, the standard deviations of the averaged amplitudes indicate the changing structure within each band rather than the uncertainties of amplitude observables.

⁹ Note that there is a different convention concerning the timestamp between geodesy and astronomy. Geocentric group delay refers to baseline group delay with a timestamp referring the geocenter.

¹⁰ See the VGOS data processing manual at ftp://ivs.bkg.bund.de/pub/vgos_corr_workshop/vgos-data-processing.pdf

measurements completely and the rests have the system temperatures measured only for a few stations and (2) the fluxes of these radio sources at the VGOS frequencies are not accurately known. In this study, the uncertainty of amplitude $\sigma(V)$ is statistically determined as the formal error of the mean amplitude by

$$\sigma(V) = \sqrt{\frac{\sum_{i=1}^L (V_i - V)^2}{L(L-1)}}. \quad (3)$$

With the amplitude V and its uncertainty $\sigma(V)$, the SNR is actually defined. The uncertainty of phase $\sigma(\phi)$ is so defined that it complies with the SNR defined by the corresponding amplitude observable.

For a triangle of three stations, a , b , and c , closure phase is defined by

$$\phi_{\text{clr}} = \phi_{ab} + \phi_{bc} + \phi_{ca}, \quad (4)$$

where, for instance, ϕ_{ab} is the geocentric phase observable on baseline ab . The closure phase uncertainty, $\sigma(\phi_{\text{clr}})$, was derived from the uncertainties of phase observables on the three baselines. With a network of M stations, there are at most $M(M-1)(M-2)/6$ closure phases available with a subset of $(M-1)(M-2)/2$ independent with each other.

With one more station d , log closure amplitude V_{clr} is defined as

$$V_{\text{clr}} = V_{abcd} = \ln \left(\frac{V_{ab}V_{cd}}{V_{ac}V_{bd}} \right), \quad (5)$$

where, for instance, V_{ab} is the amplitude observable on baseline ab . Note that the sequence of the four stations in a closure amplitude is relevant; with the same four stations, three closure amplitudes with different magnitudes can be formed. The uncertainty of log closure amplitude $\sigma(V_{\text{clr}})$, for example for V_{abcd} , is determined by

$$\sigma(V_{\text{clr}}) = \sigma(V_{abcd}) = \sqrt{\left(\frac{\sigma(V_{ab})}{V_{ab}} \right)^2 + \left(\frac{\sigma(V_{cd})}{V_{cd}} \right)^2 + \left(\frac{\sigma(V_{ac})}{V_{ac}} \right)^2 + \left(\frac{\sigma(V_{bd})}{V_{bd}} \right)^2}, \quad (6)$$

where, for instance, $\sigma(V_{ab})$ is the uncertainty of the amplitude on baseline ab as defined by equation 3. There are at most $M(M-1)(M-2)(M-3)/8$ closure amplitudes with only $M(M-3)/2$ independent ones among them.

Since the full set of closure phases—as well as closure amplitudes—is not independent, a complete noise covariance needs to be taken into account in the imaging process when the full set of closure quantities is used (Blackburn et al., 2020). In this study, we selected a subset of independent closure quantities to be used. Geodetic VLBI observations generally have high enough SNR, so we flagged out the observations with the total SNR from the combination of four polarization products lower than 25 to get rid of a small fraction of low SNR observations.

2.2 Imaging VGOS observations

The standard algorithm for astrophysical interferometric imaging is CLEAN (Högbom, 1974; Clark, 1980). It decomposes a dirty image obtained from an inverse Fourier transform of the sparsely sampled visibilities into multiple point sources and usually iterates the calibration and CLEAN processes using the information of the image obtained from the previous step, so-called “self-calibration” or “hybrid-mapping” (e.g., Wilkinson et al., 1977; Cornwell & Wilkinson, 1981; Pearson & Readhead, 1984; Thompson et al., 2017). In addition to the CLEAN algorithm, another commonly-used interferometric imaging approach, named regularized maximum likelihood (RML), solves the pixels’ fluxes of a source image by fitting directly to the data. RML applies regularization and constraints, such as entropy, sparsity, or smoothness, to solve the ill-posed problem in this imaging process (e.g., Nityananda &

Narayan, 1983; Narayan & Nityananda, 1986). It is more flexible for the RML algorithm to use different data terms, for instance, visibility phases, visibility amplitudes, closure phases, (log) closure amplitudes or various combinations of them. In the analysis presented here, we used the RML approach to make images by fitting directly closure phases and closure amplitudes¹¹ from VGOS observations. We thus can simplify the interferometric calibration process, because most calibration errors can be decoupled into station-based gain errors (e.g., Hamaker et al., 1996; Thompson et al., 2017) and thus are canceled out in closure phases and closure amplitudes. Meanwhile, apart from corrections of phase calibration systems, in the VGOS data processing additional channel-to-channel phase corrections were applied to various polarization products, but they are station-based as well. These are the reasons for using the RML imaging method to derive images from closure phases and amplitudes for VGOS observations. The eht-imaging library¹² (ehtim; Chael et al., 2016, 2018) was used to make images from the data that we generated from VGOS observations. This library constructs an objective function based on the user-specified data terms, regularizer terms and hyper-parameters and progresses toward a minimum in the objective function by using the limited-memory BFGS algorithm (Byrd et al., 1995). The ehtim library has been extensively tested for making images from closure quantities (Chael et al., 2016, 2018), and it was successfully used in making of the seminal image of the black hole shadow in galaxy M87 by Event Horizon Telescope Collaboration et al. (2019).

An automatic python script was developed to use the ehtim library based on the objective functions and iteration processes that were tested to be suitable for VGOS observations. The field of view (FOV) was 6.0×6.0 milliarcseconds (mas) with 600×600 pixels, which allows the positions of structure components to be defined in the images themselves with an accuracy better than ten microarcseconds (μas). In principle, both FOV and pixel dimensions can be increased. If the FOV increased, however, it would be time-consuming in both the imaging process and the structure-phase calculations from the images to keep the pixel spacing at ten μas . As long as the beam sizes fitted from actual observations are significantly smaller than this FOV, it is appropriate for the images of nearly all VGOS radio sources, which are selected to have compact structure.

In our RML imaging, we used the isotropic total variation regularization, which applies a smoothness constraint to the derived image and has been shown to be effective to obtain super-resolution images, about a quarter of the diffraction limit, from visibility amplitudes and closure phases (e.g., Akiyama et al., 2017); the weighting of closure phases and closure amplitudes were set to be the numbers of independent closure phases and closure amplitudes for each source. We broke the whole iteration process into several rounds with 30 or 70 times of iteration each. We started with a point source. Later on, within each round the image from the previous fitting was taken as a priori, while it was convolved with a Gaussian of the size of half of the beam size to produce the a priori model in transition to the next round. This process can help in avoiding a local minimum of the objective function. The derived images are super-resolved compared to the nominal beam size, but it has been previously shown that the RML method is capable of such super-resolution (Chael et al., 2016). This procedure was applied to derive images for all radio sources.

The direct equivalence of making images based on closure quantities and self calibration of complex visibilities was demonstrated by Blackburn et al. (2020) in both analytical and numerical ways. Even though the image derived solely from closure quantities does not have the correct flux scaling, it still has the equivalent capability as that from the self calibration technique to model source structure effects.

¹¹ We actually used log closure amplitudes.

¹² <https://github.com/achael/eht-imaging>

2.3 Imaging simulations and evaluations

To test this imaging process and evaluate the image fidelity, we simulated VLBI observations based on the super-resolution images of six sources, as listed in Table 1, from the Monitoring Of Jets in Active galactic nuclei with VLBA Experiments (MOJAVE; [Lister et al., 2018](#)), which were used as the ground truth models to evaluate the reconstructed images from the simulated data.

The simulated data were generated by assuming that they were produced by the same stations at the same epochs as the actual observations of a given source in session VO0034, but to observe the model sources at the frequency of 15.3 GHz. It produced one data set for each individual source in that session, and we did it for all the 80 radio sources one by one. As stated previously, closure quantities are insensitive to station-based errors, and it is shown by [Chael et al. \(2018\)](#) that closure-based images from the data with arbitrary levels of station-based gain errors are consistent with the tested model. It is thus only important to consider baseline-dependent errors; they were added for each simulated observation to have the same SNR as the actual observation in VO0034. We then reconstructed an image based on closure amplitudes and closure phases from each of the simulated data sets by applying the same procedure in the previous section. To quantitatively evaluate the fidelity of the derived images from these simulated data, we adopted the so-called normalized root-mean-square error (NRMSE) ([Chael et al., 2018](#)), which is a pixel-to-pixel metric and is defined as follows

$$\text{NRMSE} = \frac{\sqrt{\sum_{i=1}^J (A_i - B_i)^2}}{\sqrt{\sum_{i=1}^J (B_i)^2}}, \quad (7)$$

where A_i and B_i is the flux of the i -th pixel in image A under investigation and image B as the model, both with J pixels in total, respectively. Before computing NRMSE, both the model image and the reconstructed image were blurred with one fifth of the beam size fitted from the simulated data to have the same angular resolution and were aligned up by searching for the maximum cross-correlation between them. The simulations in [Chael et al. \(2018\)](#) showed that the NRMSE with a value of ~ 0.2 or smaller indicates an image consistent with the model.

The results with the MOJAVE image of source 0642+449 as the ground truth model are shown in Figure 1. The model image is shown in the top left corner. It has a typical structure of the geodetic VLBI sources, with a core and a jet separated by a few hundred microarcseconds (μas). The 30 images¹³ reconstructed from the simulated data set follow in the bottom. In the figure, they are sorted in the decreasing order of the number of scans with more than four stations in session VO0034. As a function of these scan numbers, the calculated NRMSE values of these images are shown in the top right corner as well as the maximum cross-correlation values. With the simulated data set equivalent to each of the 18 radio sources that were observed with more than 20 such scans, the reconstructed images have NRMSE values smaller than 0.15 and maximum cross correlations larger than 0.99. These 18 images are consistent with the model. With a few scans, however, the NRMSE values increased significantly to ~ 0.6 . With the number of scans in the range of 10–20, it is still possible to derive a reasonably good image. Similar conclusion can be made based on the simulations of the other five MOJAVE sources. These simulations preliminarily set the minimum number of scans in a 24-hour session to be 10–12 in order to make images with good fidelity, given a blind scheduling in the sense of the imaging (u, v) coverage and a similar VGOS network as in these VGOS sessions.

¹³ Even though there are 80 sources in VO0034, many of them have very few observations. There are 35 sources in VO0034 that can form closure quantities for the simulation tests here. Due to the page limit, the five images from the data sets with the least observations were not shown.

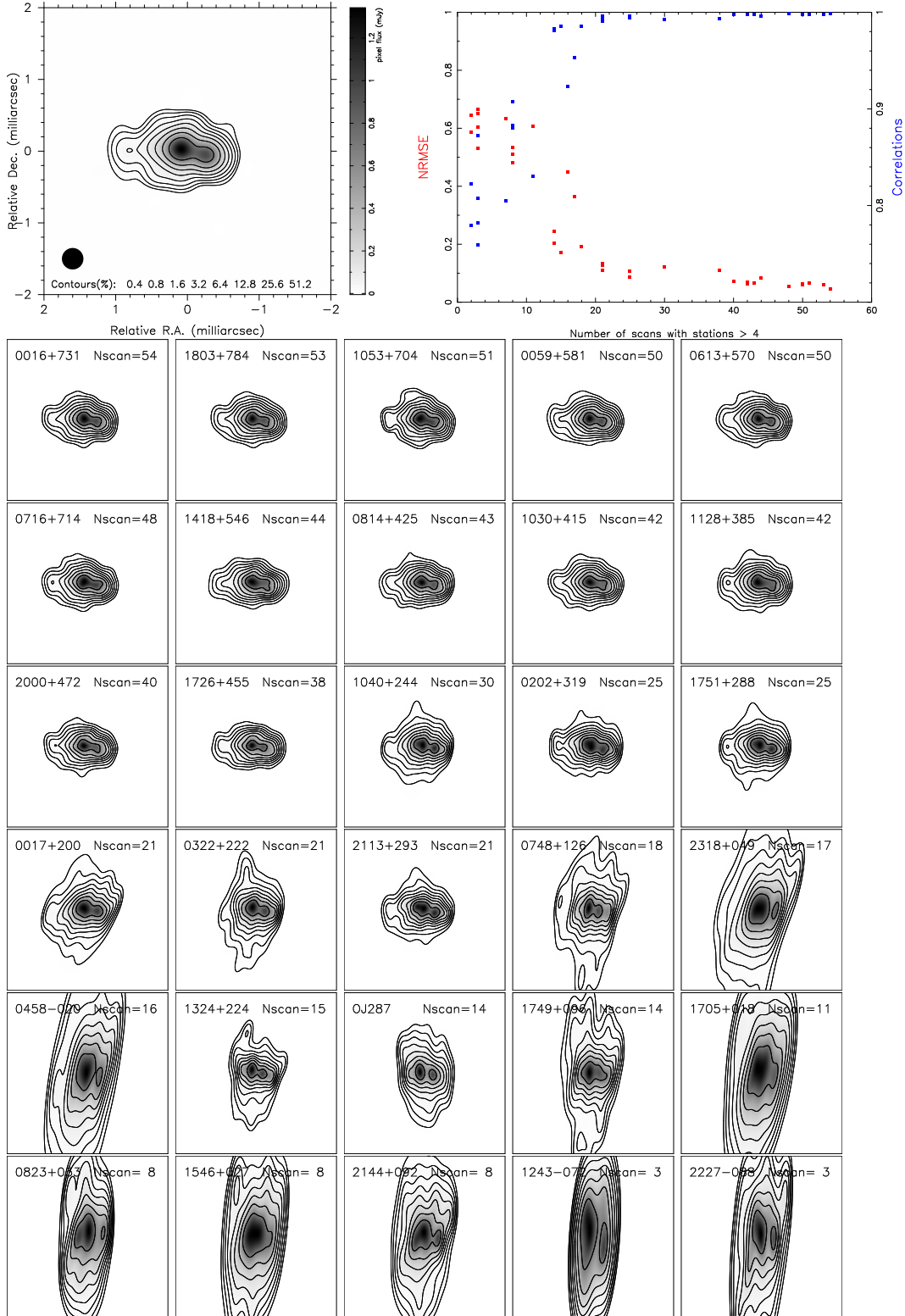


Figure 1. Reconstructed images from the 30 simulated data sets with exactly the same observing schedules as the 30 radio sources in session VO0034, based on the model input image shown in the top left corner. The 30 images are shown with the same limits of the X/Y axis as the model image. The source names are presented on the top of the 30 images together with the numbers of scans. The images from the simulated data with more than 20 scans of > 4 stations have NRMSE of about 0.1 and are consistent with the model. With more than 10 such scans, it is still possible to derive a reasonably good image.

A series of further tests were done to investigate the impact of outliers on the imaging results. For each set of the previously simulated data, one observation in the scan with more than 6 stations observing was changed by shifting its phase by 50° and its amplitude by 200%. We then produced images from these revised data. The simulations revealed that the imaging results were not significantly affected by that outlier for the data sets with more than 10 scans, because the imaging process is robust enough.

2.4 Determining structure effects in broadband observations

With the derived images at the four bands from VGOS observations, the structure effects in broadband observations can be determined through two steps: (1) calculating the structure phases at the 32 frequency channels deployed in VGOS observations (see equation 9 in Appendix 6.1); and (2) performing least-square fitting of the structure phases to derive the structure-induced delay, phase at the reference frequency and δTEC , equivalent to the process of producing broadband delays in VGOS (Cappallo, 2014, 2016). We call the second step model fitting in the paper. The structure phase at the i -th frequency channel, $\phi_{\nu_i}^{\text{str}}$, can be modeled as a function of frequency ν_i as follows

$$\phi_{\nu_i}^{\text{str}} = \tau^{\text{str}}(\nu_i - \nu_0) + \phi_{\nu_0}^{\text{str}} - \frac{k \delta\text{TEC}^{\text{str}}}{\nu_i}, \quad (8)$$

where τ^{str} , $\phi_{\nu_0}^{\text{str}}$, and $\delta\text{TEC}^{\text{str}}$ are the structure effects in broadband delay, phase at $\nu_0 = 6.0$ GHz, and δTEC observables, respectively, and are the three parameters in model fitting. Note that the structure-induced phase at the reference frequency of 6.0 GHz, $\phi_{\nu_0}^{\text{str}}$, is determined from least-square fitting while the structure phases at the 32 frequency channels in the left-hand side are calculated from images.

Figure 2 shows examples of the model fitting process for the second and forty-fourth scans of source 0016+731 on baseline GGA012M–ISHIOKA in session VO0034. The mean flux positions, which are the centers of the images in Figure 4, were used as the reference points to calculate the structure phases at the 32 channels. The uncertainties of these three parameters were obtained together from least-square fitting as well. Large uncertainties, which indicate a poor fit to the structure phases, can result from large across-band variations in structural phases due to significantly different structure between the four bands or the misalignment of the images. For the case of source 0016+731, the residuals were at the level of a few degrees or even smaller by using the mean flux points as the references.

2.5 Selecting reference points in the images at the four bands

The reference point in an image itself is critical in modeling source structure effects, because it will immediately affect the derived source position from geodetic VLBI analysis, in which the structure models are introduced. In VGOS observations, the reference point shall require not only a stable point in the source structure over time but also the accurate alignment of the images across the four bands as the actual radio emission of the source. In addition to the mean flux point previously used, the maximum flux point is another reference point that is also easily accessible in an image. The impact of the alignment between the images at the four bands can be demonstrated by applying these two types of reference points to derive structure effects and comparing. Figure 3 shows two equivalent plots to those in Figure 2 but using as the references the maximum flux points, the coordinates of which in Figure 4 are $(-0.216, 0.176)$, $(-0.240, 0.164)$, $(-0.229, 0.105)$, and $(-0.189, 0.063)$ mas for the four bands, respectively.

As we can see from Figures 2 and 3, the modeled structure effects in VGOS group delays, δTEC and phase offsets at the reference frequency are highly dependent on the reference points used. The residuals of least-square fitting for these two cases are also different, which leads to different uncertainties of the three parameters. For source 0016+731 the fitting is

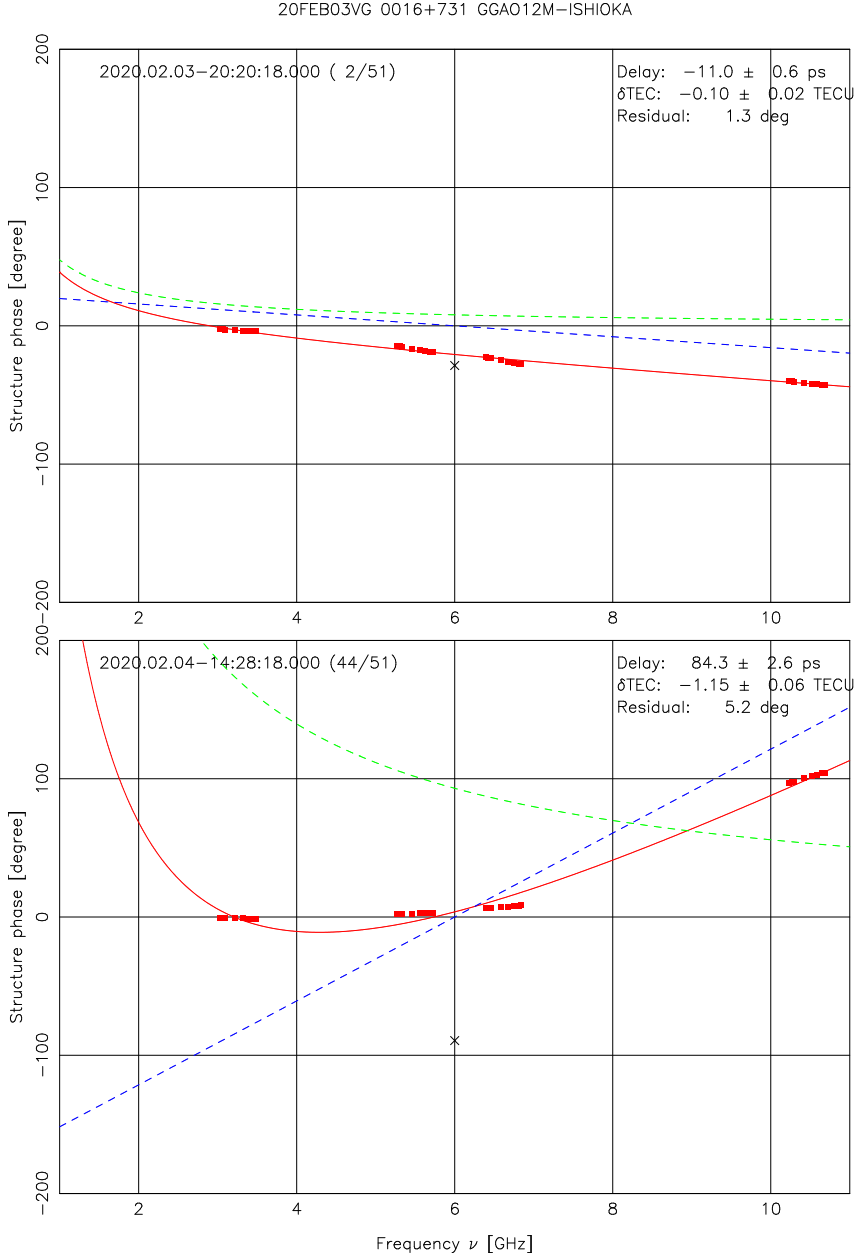


Figure 2. The structure effects on VGOS observables derived through model fitting of the structure phases calculated by using the closure-based images and referring to the mean flux points in the four-band images. The upper plot is for the second scan of source 0016+731 on baseline GGA012M-ISHIOKA in session VO0034, and the bottom plot for the forty-fourth scan. Structure phases at the 32 channels in red dots are calculated from the images shown in Figure 4. Dashed blue line and dashed green line are the best-fit group delay and δ TEC model from least-square fitting, respectively; black cross on the vertical line of 6.0 GHz is the best-fit phase offset. The combined model from these three parameters is shown as the full red line. The estimated values of the structure-induced delays and δ TEC are presented in the upper-right corner of each plot together with their uncertainties. The post-fit residuals of these two scans are 1.3° and 5.2° , respectively, and they are also shown in the plots.

better when the mean flux points are used as the references. This is usually the case for many other sources.

We note that there is no warranty that either of these two reference points can align up the images at the four bands or be a stable point on the sky over time. The mean flux point can change significantly over time and/or from band to band when the structure evolves with time and/or frequency. The maximum flux point can exchange between the jet and the core at different bands and/or times. Meanwhile, due to core shift, which will be discussed in section 4.2, it is unlikely that the maximum flux point can be used to align the images accurately. However, our study suggests that even though the misalignment of the images at the four bands significantly influences the model fitting shown in the previous section, it does not affect the sum of those model values over a triangle, named modeled closures. Two exceptions to this are that the uncertainties of modeled closures and jumps in modeled closures may change—these will be demonstrated and discussed later. Therefore, we can temporarily rely on these two accessible reference points for our analysis here. For the analysis in the next section, the mean flux points were used as the references in the images.

3 Results

3.1 Imaging results

As an example of moderate structure, the images of source 0016+731 obtained from the VGOS session VO0034 are shown in Figure 4. The images show its extended structure at the four bands along the position angle of $\sim 110^\circ$. Since VGOS observations at the four frequencies are made simultaneously, their array configuration is the same and therefore the angular scales probed decrease linearly with the increasing frequency. The angular scales of the core decrease when the frequencies go higher, however, the entire structure (the core and the extended jet) has similar extent at the four bands. The structure effects in broadband group delay observables of this source were predominantly due to its structure at higher frequencies.

These four images were constructed from 645 independent closure phases and 801 independent closure amplitudes at each of the four bands. The reduced χ^2 , which is a metric to evaluate the goodness of fit, of the closure phases is 0.79, 1.12, 1.02, and 1.10 for the four bands, respectively; that of the log closure amplitudes is 1.04, 0.59, 0.86, and 0.89. They are approximately unity suggesting that the fitting was performed well and the uncertainties of the amplitudes and phases were reasonably determined. In total, there are 6181 closure amplitudes (at each of the four bands) with the root-mean-square (RMS) values of 0.43 at 3.3 GHz, 0.65 at 5.5 GHz, 0.80 at 6.6 GHz, and 0.87 at 10.5 GHz; by subtracting the modeled log closure amplitudes, the RMS values of the residuals are 0.11, 0.07, 0.08, and 0.12, respectively. Figure 5 shows the observed log closure amplitudes in blue dots and the modeled log closure amplitudes in green open circles for the quadrangle GGA012M–ISHIOKA–MACGO12M–ONSA13SW. The error bars of observed log closure amplitudes were calculated from the derived uncertainties of amplitude observables on the four baselines of each individual closure as defined by equation 6. The comparison of closure phases are shown in Appendix 6.2. Source 0016+731 is one of the sources that have moderate structure among the sources frequently observed in VGOS observations.

Images for other representative sources are shown in Appendix 6.3. Direct comparison was made for six sources between our VGOS images and the MOJAVE images, which were obtained by astronomical arrays that have a good calibration and good (u, v) coverage. The figures are shown in the Appendix 6.4. For the comparison, the VGOS images were constrained to have the same total fluxes as the corresponding MOJAVE images.

Since images with different resolutions contain structure at different angular scales, we used the Gaussian beams of two different sizes to convolve both the VGOS images and MOJAVE images before the image comparison, the full beam size of the VGOS image under

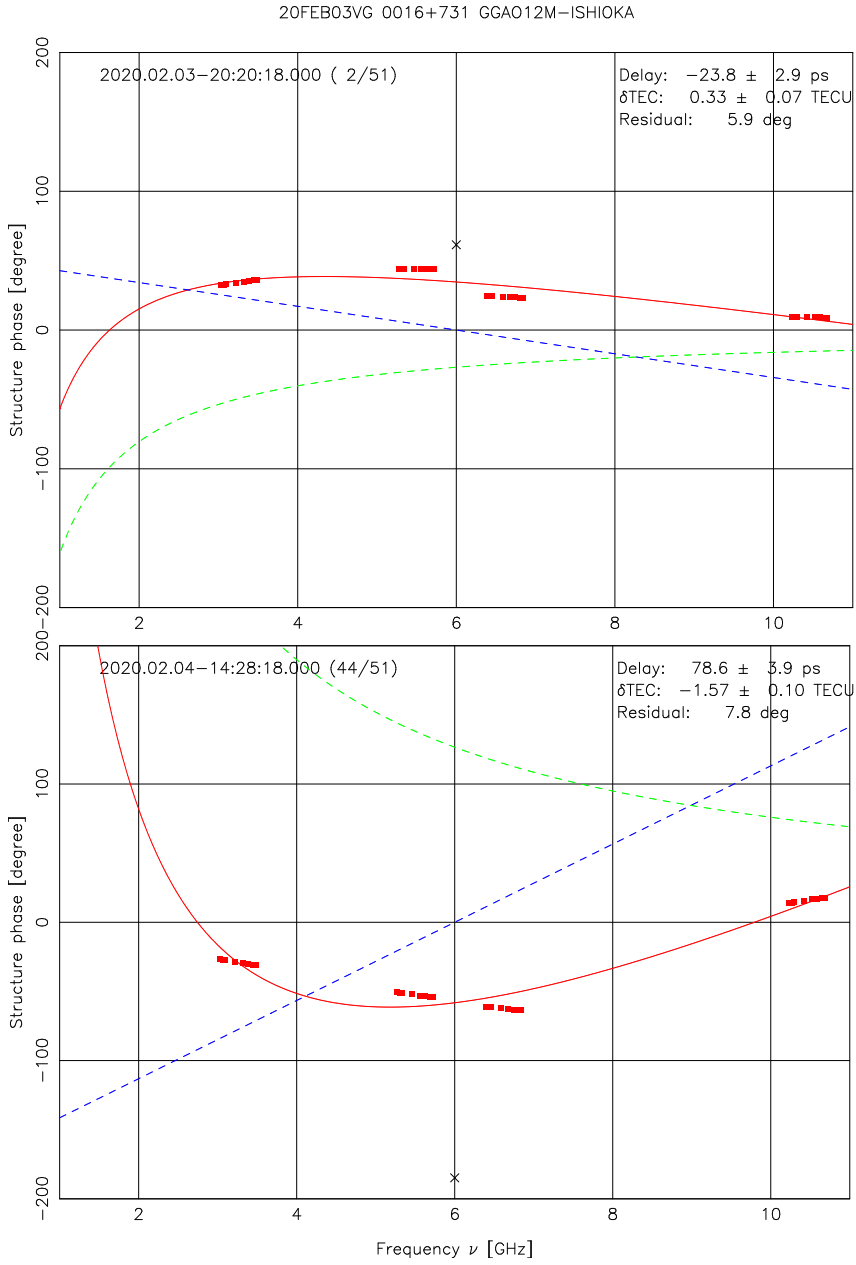


Figure 3. Equivalent plots to Figure 2 but referring to the maximum flux points in the images to calculate the structure phases at the 32 channels. The coordinates of these reference points are presented in Figure 4. The post-fit residuals of these two scans are 5.9° and 7.8° , respectively. See Figure 2 for a description of the plot.

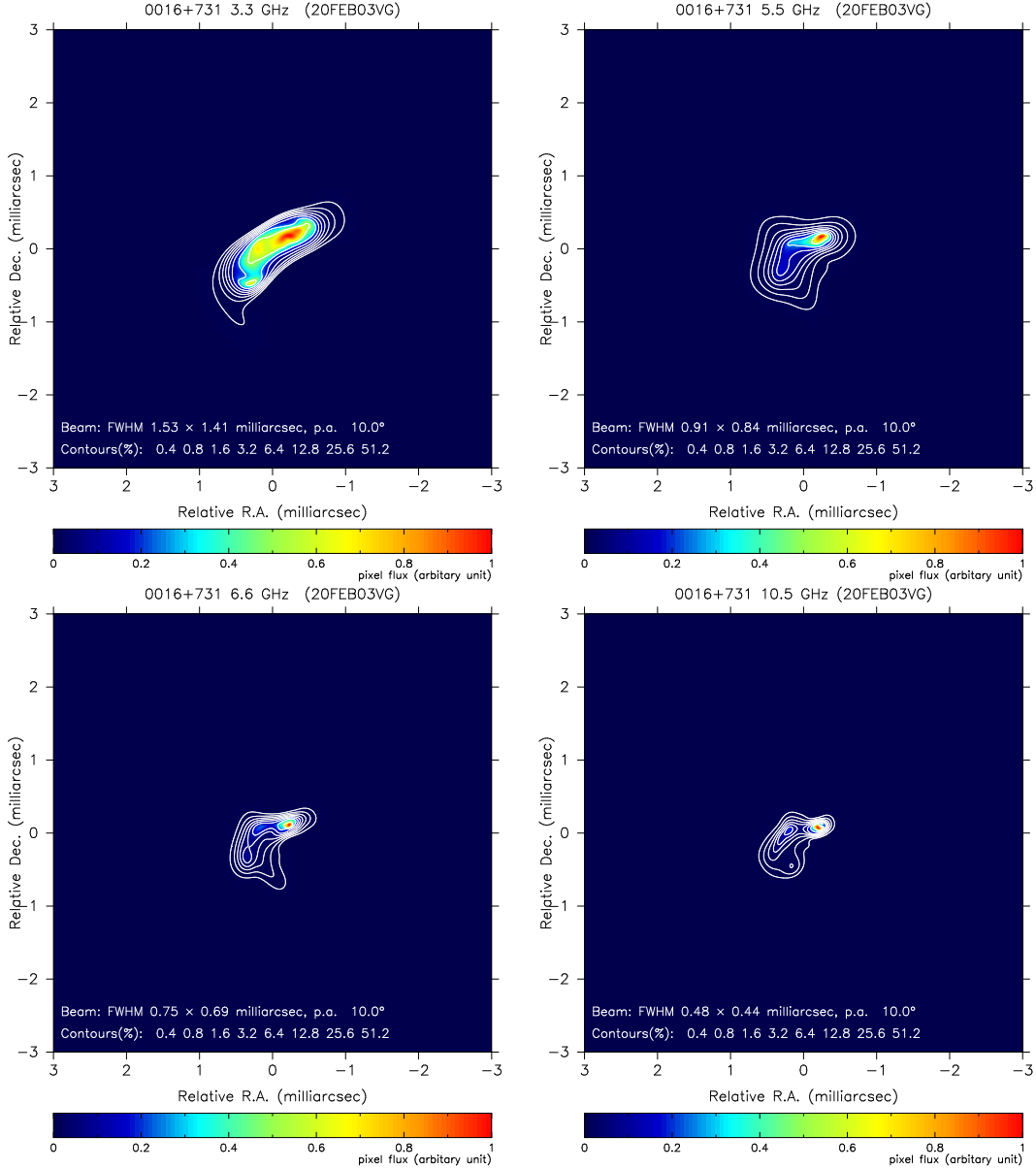


Figure 4. Closure-based images of source 0016+731 at the frequencies of 3.3 GHz, 5.5 GHz, 6.6 GHz, and 10.5 GHz from VGOS observations VO0034. Overlay contours are shown at eight levels of peak percentage (specified in the bottom of plots) in white. They were derived based on closure phases and closure amplitudes only, therefore, information of the absolute source positions and the total flux densities was missing. The mean flux positions were chosen as the centers for the plots and the pixel fluxes are in arbitrary units. The coordinates of the maximum flux points are $(-0.216, 0.176)$, $(-0.240, 0.164)$, $(-0.229, 0.105)$, and $(-0.189, 0.063)$ mas in the four-band images, respectively. The convolution beam parameters are shown in the bottom of each plot.

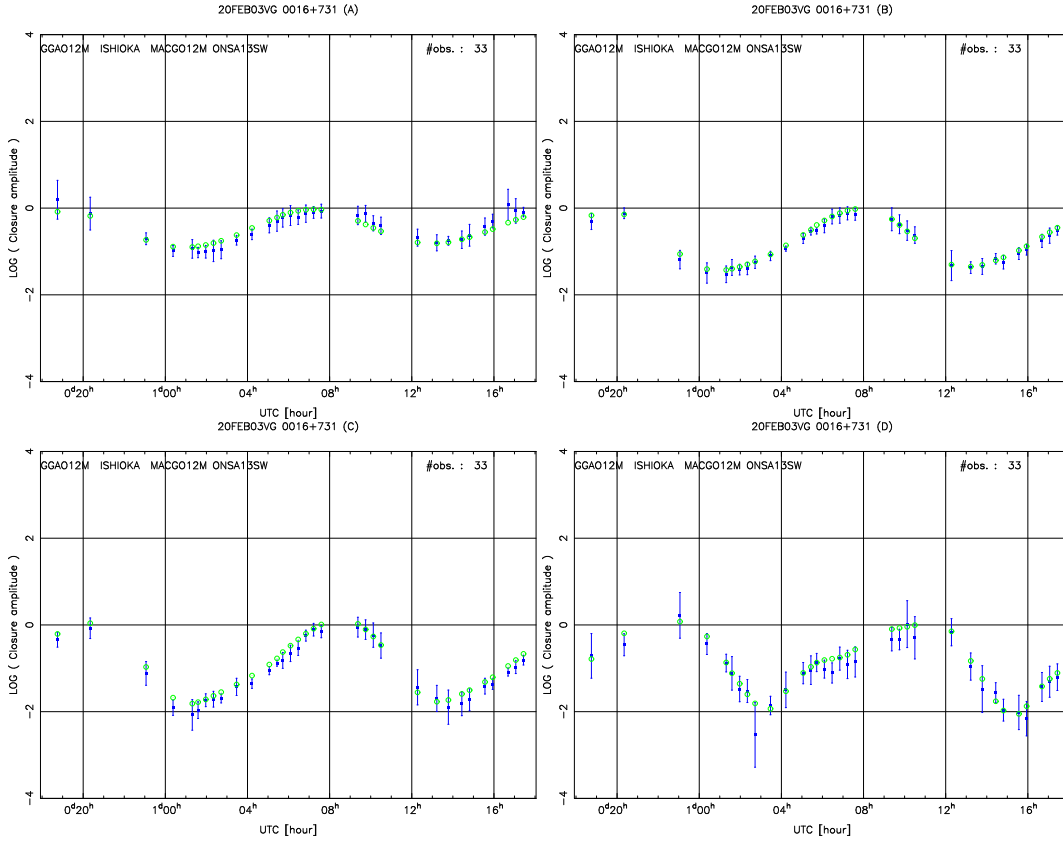


Figure 5. Observed log closure amplitudes (blue dots) and modeled log closure amplitudes (green open circles) of quadrangle GGAO12M–ISHIOKA–MACGO12M–ONSA13SW for source 0016+731 at the frequencies 3.3 GHz (upper-left), 5.5 GHz (upper-right), 6.6 GHz (bottom-left), and 10.5 GHz (bottom-right) in session VO0034. The RMS values of the log closure amplitudes of this quadrangle are 0.58, 0.94, 1.24, and 1.18 at the four bands, respectively; by subtracting the modeled log closure amplitudes, the corresponding RMS values of the residuals are 0.15, 0.08, 0.15, and 0.16.

investigation and one fifth of that beam size. The full-beam resolution allows us to compare large-scale structure whereas the over-resolved approach can tell the difference in fine-scale structure. The cross correlation and NRMSE values of the comparison for the full beam-size convolved images are shown in Table 1. In this case, the correlation is often very high, larger than 0.95, and around half of the VGOS images have NRMSE values of 0.2 or smaller. It suggests that at large scales the VGOS images are consistent with the MOJAVE images. In general, the NRMSE values for VGOS images at higher frequencies are significantly larger than that for the ones at lower frequencies, probably mainly due to the finer angular resolutions at the higher frequencies. Table 2 shows the results of comparing the images convolved with the smaller beam sizes. In this case, all the NRMSE values are significantly larger than 0.2, which tells that they have quite different structure at fine scales. If we take source 1030+415 as an example, the MOJAVE image shows only a dominant core, while the VGOS images at the two higher-frequency bands clearly reveal it has a strong jet away from the core by approximately an angular distance of the beam size; we will discuss in the next subsection further the strong structure effects caused by its structure within the beam size. The VGOS images were consistent with the MOJAVE images when convolved with the full beam sizes, but were significantly different when convolved with much smaller beam sizes. There are two possible reasons: (1) the RML algorithm is better at deriving images with higher resolutions and (2) radio sources have more prominent jet structure at the lower frequency bands, which is always true for synchrotron jets. Therefore, the NRMSE values were really small when the large-scale structure was compared, and they considerably increased when the fine-scale structure was evaluated. However, by comparing the structure phases calculated based on the images convolved with these two different beam sizes, it is found that the fine-scale structure is important for VGOS observations to model source structure effects, as already discussed by [Porcas \(2010\)](#).

Table 1. Statistics of the comparison between our results and MOJAVE images when convolved with the corresponding beam sizes of VGOS images

Source	3.3 GHz		5.5 GHz		6.6 GHz		10.5 GHz	
	Corr.	NRMSE	Corr.	NRMSE	Corr.	NRMSE	Corr.	NRMSE
0016+731	0.998	0.09	0.990	0.17	0.984	0.20	0.958	0.31
0642+449	0.995	0.13	0.975	0.25	0.960	0.31	0.910	0.43
1030+415	0.999	0.07	0.997	0.13	0.995	0.16	0.986	0.24
1418+546	0.970	0.28	0.968	0.29	0.964	0.31	0.946	0.37
1803+784	0.994	0.13	0.983	0.21	0.979	0.23	0.971	0.27
3C418	0.985	0.24	0.950	0.40	0.916	0.47	0.812	0.63

3.2 Closure delays

Based on the derived images and model fitting, structure-induced delays, δTEC , and phase offsets at 6.0 GHz were determined together with their uncertainties. They were used to calculate modeled closures, which were compared with the observed closures. The comparisons of closures temporarily avoid the difficulty of properly aligning up the images.

3.2.1 Source 0016+731

For the 1883 closure delays of source 0016+731 in session VO0034, the RMS is 24.9 ps; by subtracting the modeled closure delays, it reduces to 5.5 ps only. A magnitude of 24.3 ps in the variation of the observed closure delays for this source is explained by its structure effects. Figure 6 shows its observed and modeled closure delays for two triangles GGA012M-ISHIOKA-ONSA13SW and ISHIOKA-MACG012M-ONSA13SW as examples to demonstrate this.

Table 2. Statistics of the comparison between our results and MOJAVE images when convolved with one fifth of the corresponding beam sizes of VGOS images

Source	3.3 GHz		5.5 GHz		6.6 GHz		10.5 GHz	
	Corr.	NRMSE	Corr.	NRMSE	Corr.	NRMSE	Corr.	NRMSE
0016+731	0.922	0.40	0.890	0.47	0.882	0.48	0.869	0.50
0642+449	0.856	0.52	0.800	0.60	0.793	0.61	0.785	0.62
1030+415	0.962	0.34	0.918	0.44	0.903	0.48	0.875	0.52
1418+546	0.928	0.41	0.913	0.45	0.910	0.46	0.903	0.47
1803+784	0.959	0.30	0.939	0.35	0.932	0.37	0.914	0.41
3C418	0.757	0.70	0.711	0.74	0.697	0.75	0.670	0.77

Similar to the closures from the traditional S/X VLBI observations, the closures of broadband group delays determined from the process in section 2.4 have the feature that they are insensitive to the reference points in source structure at any of the four bands. Even though closure delays involve three baselines, which leads to difficulty in interpretation of source structure effects, they are still instructive to understand those effects on each of the three baselines. There are three pairs of positive and negative peaks separated by 12 hours in both plots; each of the three pairs of positive and negative peaks correspond to the structure effects on each of the three baselines. The structure effects of source 0016+731 cause errors on the baselines in the plots with magnitudes of about 50 ps, which do not include the effects of a possible source position shift due to its structure.

3.2.2 Source 1030+415

The images of source 1030+415 are shown in Figure 20. At the three higher frequencies, two components separated by ~ 1 mas are visible. The relative flux ratio of the two components gets stronger when the frequency increases, which leads to much larger structure effects at higher-frequency bands. For its 813 closure delays in the session VO0034, the RMS is 50.2 ps, and the RMS residual is 10.1 ps by correcting them based on the images. Significant amount of systematic errors due to structure effects can be reduced by using the images. Figure 7 shows its structure effects on triangle KOKEE12M-ONSA13SW-WESTFORD. The model curve predicts well the observed closure delays. It has larger and more complicated structure effects compared to source 0016+731.

There are two jumps in closure delays at about 09:00 and 13:00 UTC, as indicated by the continuous model curve. They were caused by shifts of 2π in the structure phases at 10.5 GHz before those two epochs. The jumps will be studied further in section 3.5.

3.3 Closure δ TEC

The sum of δ TEC estimates over a loop of three stations, called closure δ TEC, uncovers systematic errors in δ TEC estimates. The ionospheric effects are station-based, and thus are closed along the loop of a triangle. Since source structure itself and its effects are frequency-dependent, and so far they are not corrected in channel visibility phases used for fitting the δ TEC observables, the actual δ TEC observables are affected by these effects, causing non-zero closure δ TEC values. Based on our imaging results, source structure effects on δ TEC can also be studied and quantified by forming modeled closure δ TEC. Figure 8 shows the

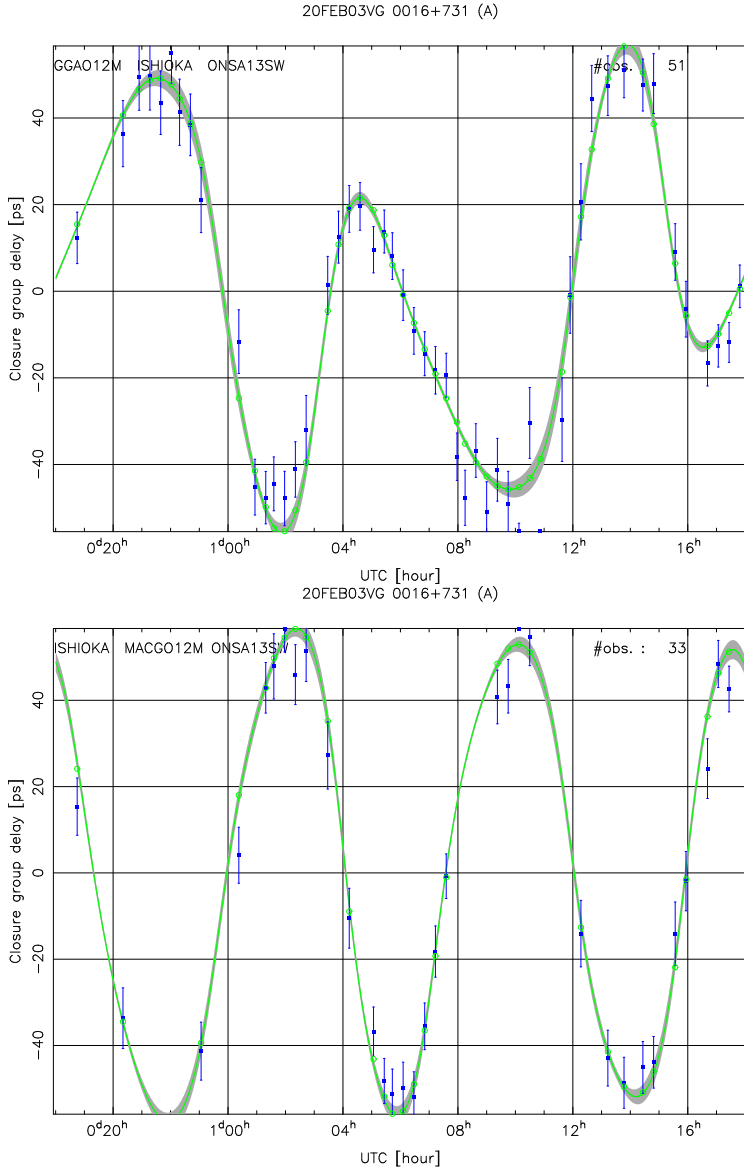


Figure 6. Observed closure delays (blue dots) and modeled closure delays (green open circles) of two triangles GGAO12M–ISHIOKA–ONSA13SW (upper) and ISHIOKA–MACGO12M–ONSA13SW (bottom) for source 0016+731 in session VO0034. The continuous model curve is shown as the green line and the 1- σ errors are in gray. The RMS closure delays of these two triangles are 34.2 ps (upper) and 40.5 ps (bottom), and the RMS residuals are both 6.5 ps.

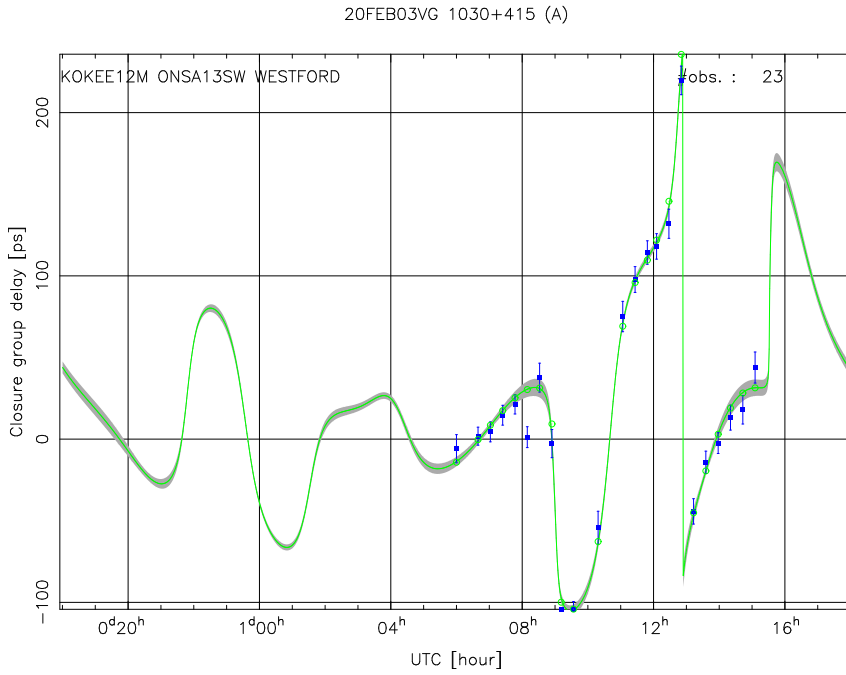


Figure 7. Observed closure delays (blue dots) and modeled closure delays (green open circles) of triangle KOKEE12M–ONSA13SW–WESTFORD for source 1030+415 in session VO0034. The continuous model curve is shown as the green line and the $1\text{-}\sigma$ errors are in gray. The RMS closure delay of this triangle is 78.7 ps, and the RMS residual is 10.1 ps by subtracting the modeled closure delays from the observed ones. There are two jumps in closure delays with magnitudes of more than 100 ps at about 09:00 and 13:00 UTC.

observed closure δTEC and modeled closure δTEC^{14} on the triangle ISHIOKA–WESTFORD–WETTZ13S for source 1418+546 and on the triangle ISHIOKA–KOKEE12M–WETTZ13S for source 1803+784. The images of these two sources are shown in Figures 21 and 14, respectively. The systematic errors in δTEC observables from VGOS observations can be significantly reduced by correcting source structure effects. As we have seen, it is common that structure effects cause systematic errors at the level of 1 TECU on VGOS δTEC observables. Attention must be paid to use of these δTEC observables.

3.4 Comparison of structure effects on broadband and single-band delay observables

Structure effects in VGOS broadband delays were compared with the effects in single-band delays derived from the structure model and the image at that band only (see equations (9) and (10) in Appendix 6.1). However, this kind of comparison makes sense only for the sources with minimum or moderate structure. For sources with extended structure, there are 2π ambiguities of the structure phases between different bands, which can lead to complicated structure effects. The structure effects in VGOS broadband delays for those extended sources will be discussed in the next section.

Figure 9 shows the structure effects on VGOS broadband delays and single-band delays at each of the four bands for three sources 0016+731, 1053+815, and 1803+784. If the structure effects at the highest frequency band are larger than that at the other bands, as shown in the upper and middle panels, they will dominate the structure effects in broadband delays. The structure effects at the lowest frequency band, however, are largely suppressed in broadband delays as demonstrated by the bottom plot for source 1803+784. On the contrary, the large structure effects at the lowest frequency band are absorbed by δTEC observables leading to significant variation in closure δTEC as shown in the bottom plot of Figure 8 for this source.

In general, broadband delays have structure effects with smaller magnitudes than the single-band delays with the largest magnitudes among the four bands. On the other hand, the source structure effects in VGOS involve source structure at the four frequency bands simultaneously, whereas in S/X VLBI observations these effects at the two bands can be modeled and studied independently as single-band delays. For S/X VLBI observations, one could even ignore the structure effects at the S band; whereas for VGOS observations, an ignorance of structure effects at one band or a misalignment of the images at the four bands could lead to completely different results in modeling.

3.5 Delay/ δTEC jumps

Jumps in the delay and δTEC observables were reported by Xu et al. (2020). These jumps are confirmed to be caused by source structure effects in this study by comparing observed closures to modeled closures. Taking as an example, Figure 10 shows observed and modeled closure delays of triangle GGA012M–ONSA13SW–RAEGYEB for source 3C418 in session VT9217, the images of which are shown in Figure 18. When uncertainties of the modeled closure delays are smaller than about 10 ps, the modeled closure delays agree with the observed ones very well. However, when uncertainties of the modeled values are large, the observed closure delays deviate from the modeled ones by several hundreds of picoseconds.

These jumps are found to be caused by large variations in phases between the four bands due to source structure effects. In the cases of extended sources, the frequency separations between the four bands are large enough for their structure effects to produce phase differences larger than 2π between various bands. Without correcting structure phases

¹⁴ Note that modeled closure δTEC is the negative of the sum of structure-induced δTEC on three baselines based on equation (8) in order to follow the sign of the observed closure δTEC .

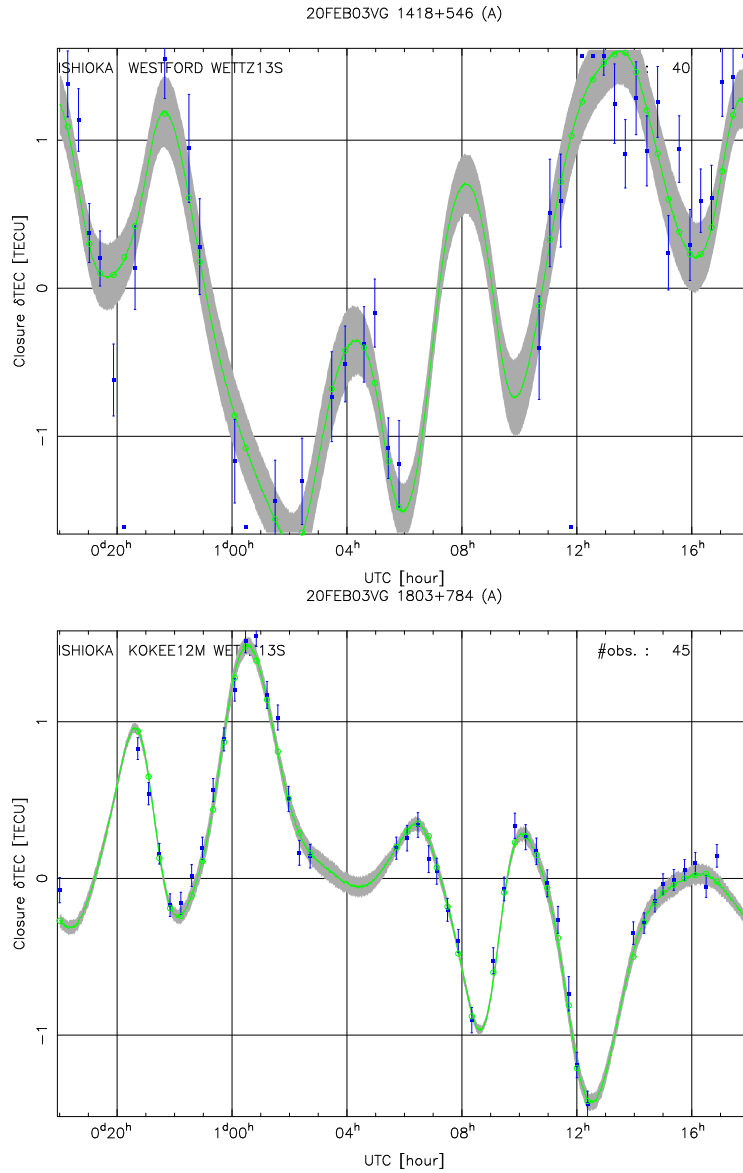


Figure 8. Observed closure δ TEC (blue dots) and modeled closure δ TEC (green open circles) of triangle ISHIOKA–WESTFORD–WETTZ13S for source 1418+546 (upper) and of triangle ISHIOKA–KOKEE12M–WETTZ13S for source 1803+784 (lower) in session VO0034. The continuous model curve is shown as the green line and the 1- σ errors are in gray. The RMS values of closure δ TEC are 1.10 TECU (upper) and 0.62 TECU (lower), and the RMS residuals are 0.39 TECU (upper) and 0.09 TECU (lower).

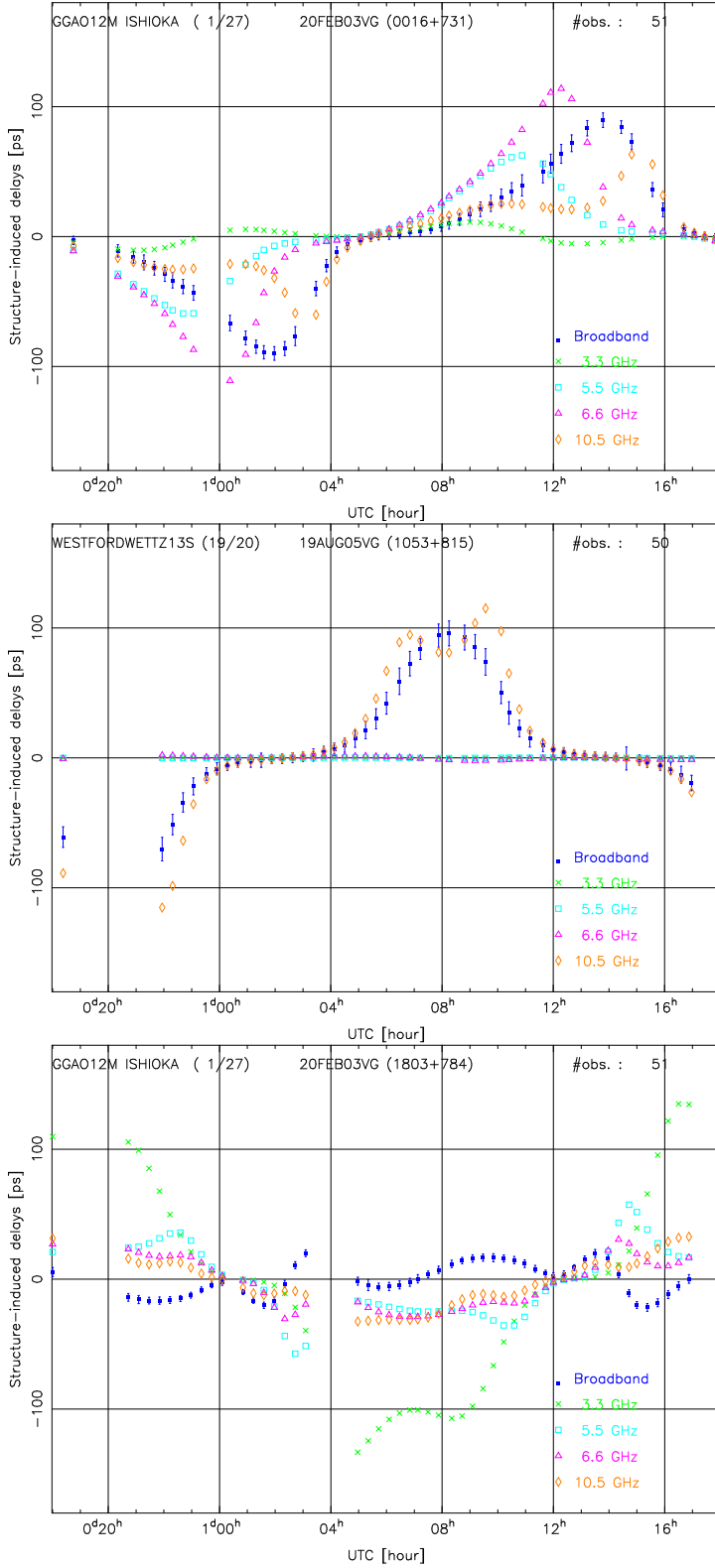


Figure 9. Comparison between the structure effects on VGOS broadband delays and single-band delays at the four bands for three sources 0016+731 (top), 1053+815 (middle), and 1803+784 (bottom). The structure effects in broadband delays are determined from the process in section 2, while the effects in single-band delays are calculated based on the model and the image at that individual band only. These model points are associated with the actual observations in session VO0034 or session VT9217.

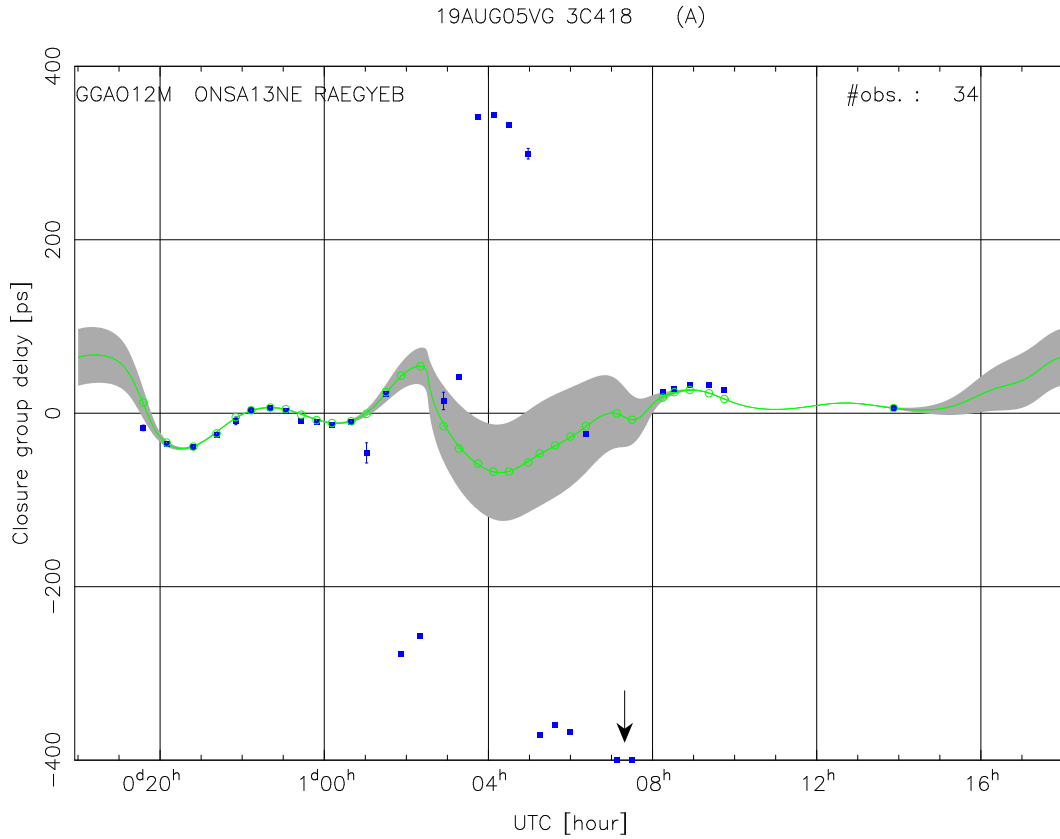


Figure 10. Observed closure delays (blue dots) and modeled closure delays (green open circles) of triangle **GGA012M–ONSA13SW–RAEGYEB** for source **3C418** in session **VT9217**. The continuous model curve is shown as the green line and the $1\text{-}\sigma$ errors are in gray. Two observed closure delays of about -720 ps, pointed by the arrow, are shown on the bottom axis.

in the process of producing VGOS broadband delay and δTEC , such phase ambiguities between the four bands may not be successfully resolved. Model fitting to the structure phases on baseline GGA012M-ONSA13NE for one of the scans with delay jumps shown in Figure 10 is demonstrated in figure 11. There are three possibilities to do model fitting for this scan: (1) wrapping all the phases in the range of -180° to 180° (the upper plot); (2) shifting the phases at the second band by -360° (the middle one); and (3) shifting the phases at the third band by 360° (the bottom one). The difference in delay estimates between the first and second scenarios is about -355 ps and that between the first and third scenarios is about 327 ps. Since the triangle GGA012M-ONSA13SW-RAEGYEB involves another long baseline GGA012M-RAEGYEB, the delay jumps in its closure delays thus can have spacing with various combinations of those two values or two times of one of them. More complicated jumps are found in closure delays for those larger triangles. Delay jumps in the observations of other sources like 0642+449, 1030+415, 1418+546, and 2000+472 are explained by their structure effects as well. Their images are shown in Figures 19, 20, 21, and 22, respectively. The jumps in δTEC observables are caused by the same reason. It is obvious that these observations with large jumps can finally be recovered if structure phases are taken into account in the VGOS data processing.

4 Discussion

4.1 Impact of the reference points on the source structure

By referring to different points in the four-band images, the model fitting gives completely different model values; however, the modeled closure values remains unchanged except when the jumps in the modeled delay/ δTEC values happen. The reason is that the differences between the model values of structure-induced delays from different reference points form sinusoidal waves, which can be modeled by a common source position offset for all the baselines and thus be canceled out exactly in closures. This is shown in Figure 12 for the observations of sources 0016+731 and 1030+415. The structure effects of source 1030+415 change more rapidly than those of source 0016+731 but the differences between the model values still follow a sinusoidal wave. These differences for the observations of source 0016+731 on the 27 baselines in session VO0034 can be modeled perfectly by a position offset $(-0.037, -0.093)$ mas and that of source 1030+415 by a position offset $(-0.678, -0.202)$ mas. Neither of these two cases can be easily inferred from the position offsets between the two types of reference points used. The misalignment between the images at the four bands would cause variations in derived source positions from geodetic VLBI solutions. The dependence of the source position determined by broadband group delays on the reference points at the four-band images requires further investigations. Due to the strong correlation between broadband delays and δTEC (Cappallo, 2015; Xu et al., 2020), systematic differences with the same pattern as the differences in modeled broadband delays will happen to modeled δTEC values; thus, external information on δTEC with an accuracy better than 0.5 TECU may help in aligning up the images.

For sources with moderate structure, if the jet position angles at various bands are along the same direction, which is validated for most of VGOS sources, the structure phases at the 32 channels are always in phase by referring to the mean flux points—zero structure phases at the four bands tend to happen at the same epochs as well as the maximum and minimum phases. This in-phase feature leads to a good model fitting and thus small uncertainties of the parameters as shown in Figure 2. But the choices of other reference points result in additional phase offsets between the four bands, leading to structure phases at the 32 channels out of phase and thus larger uncertainties of the parameters. For sources with complicated structure, the structure phases at the 32 channels are always out of phase even by referring to the mean flux points, as we can see in Figures 10 and 11. The large variations in structure phases at different bands, which cause the jumps, may happen at different periods of time by referring to different reference points. However, apart from

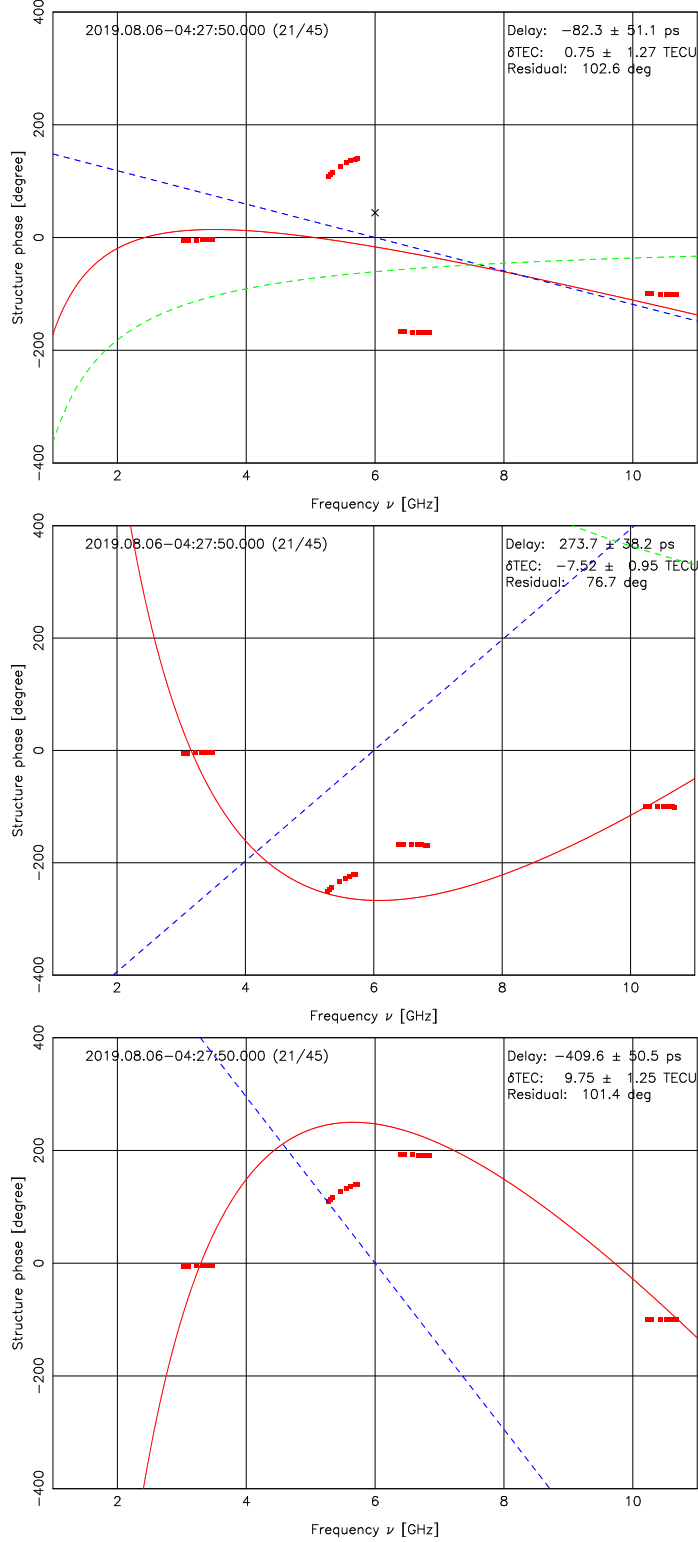


Figure 11. Three possible scenarios of model fitting to the structure phases at the 32 channels on baseline GGA012M–ONSA13NE for the twenty-first scan of the source 3C418 in session VT9217. The case of wrapping the structure phases in the range of -180° to 180° is shown in the upper plot. The middle plot is the case of shifting the structure phases at the 8 channels around 5.5 GHz by -360° and the bottom one shifting the structure phases at the 8 channels around 6.6 GHz by 360° . This large variation in structure phases leads to unpredictable jumps in delay and δTEC observables.

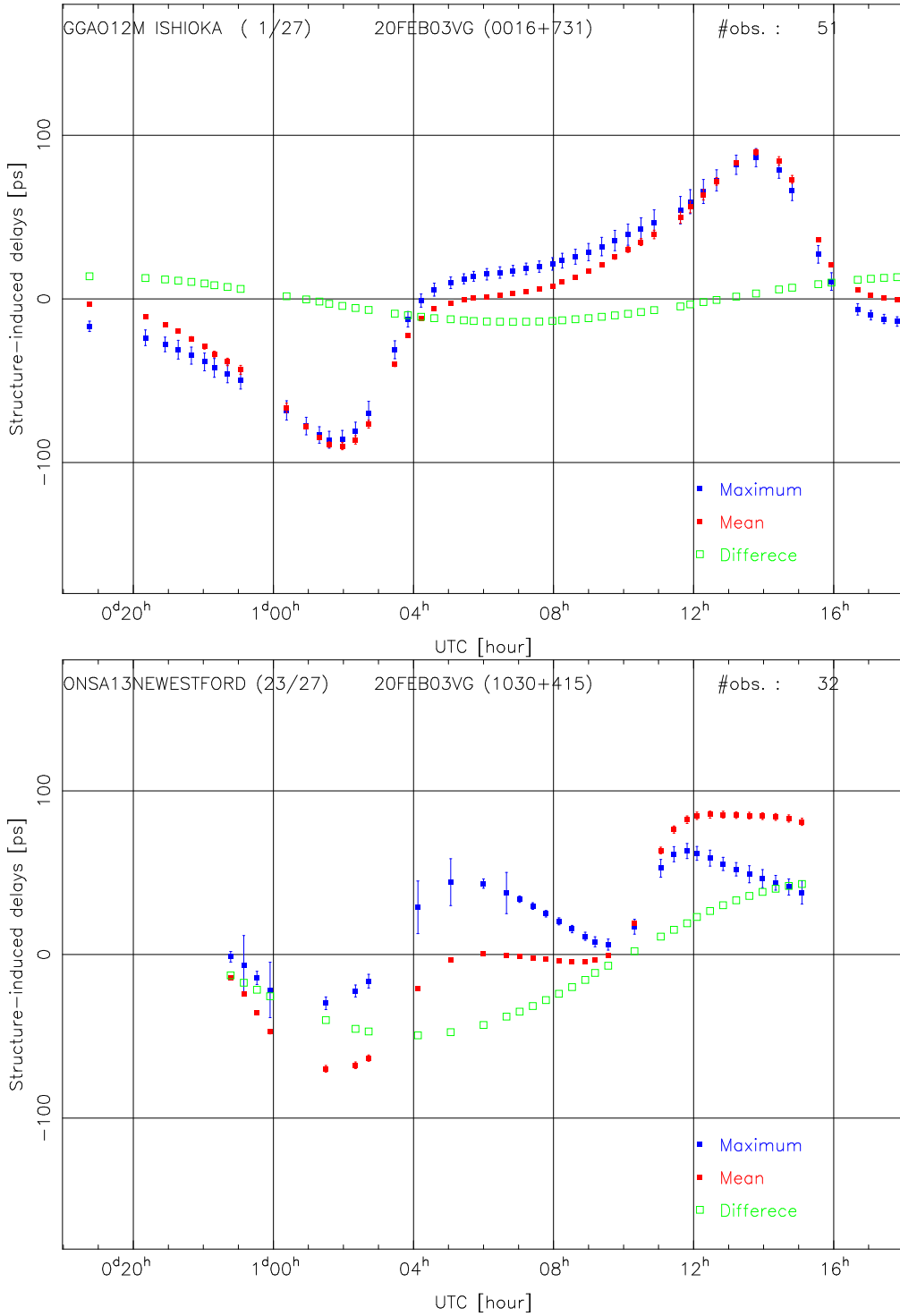


Figure 12. Structure-induced delays in VGOS broadband observations of source 0016+731 (upper) and of source 1030+415 (bottom) based on the images by referring to the maximum flux points and the mean flux points in their images. The differences between them are shown in green rectangles. The error bars of the model values are their $1\text{-}\sigma$ errors from model fitting. By referring to the mean flux points in the images, model delays always have smaller uncertainties.

the jumps, the modeled closures of the extended sources do not change with the different reference points used.

Equivalent to the impacts of misalignment of the images, the derived source positions from geodetic solutions are dependent on the actual source positions at the four bands, which can be different due to different structure and core shift (it will be discussed in section 4.2.). For traditional S/X VLBI observations, derived source positions are dominated by that at X band, while for VGOS observations, where group delay and δ TEC observables are estimated simultaneously, that dependence has changed to be complex.

4.2 Impacts of core shift

What we call the “core” in the VLBI images of active galactic nuclei jets at centimeter wavelengths is in fact the synchrotron photosphere, i.e., the point at which the jet becomes optically thin at the given frequency. As predicted by [Blandford & Königl \(1979\)](#) the position of the core along the jet is frequency-dependent with the core moving upstream with increasing frequency. The effect has been measured by using quasi-simultaneous multi-frequency VLBI observations (e.g., [Kovalev et al., 2008](#); [Sokolovsky et al., 2011](#); [Pushkarev et al., 2012](#); [Plavin et al., 2019](#)). A series of simulations with different dependence of core shift on the observing frequency has been performed for several sources in this study. As discussed by [Porcas \(2009\)](#), in the case that core shift is a function of the observing frequency with the power of -1 , group delays measure the source positions at the jet base rather than the actual positions where the radio signals were emitted. This is because the core shift effect with a dependence of the power of -1 on the observing frequency ν causes a constant phase over frequency, which will be absorbed by ϕ_{ν_0} with the other two parameters unchanged in model fitting. If the core shift dependence on frequency deviates from the power of -1 , it will cause variations in baseline-based group delays and δ TEC. In other words, source positions change and the study of VGOS δ TEC using external information about the ionospheric effects may detect the part of core shift deviating from the function of ν^{-1} , if any. In the case of the effects due to the relative angular structure are determined as shown by the imaging results, the remaining part of core shift effect is merely source position shift between the four bands that have been discussed in the last section. To determine the core shift would need different measurements than closure quantities.

The radio core-shift was determined for a number of sources by referring to the bright compact features in the optically thin, extended jet in astrophysical imaging. This method is named “self-referencing” technique and has been used by a series of studies (e.g., [Kovalev et al., 2008](#); [Sokolovsky et al., 2011](#); [Pushkarev et al., 2012](#); [Plavin et al., 2019](#)). Relative astrometrical VLBI, the so-called phase referencing technique, nowadays approaches relative positional accuracies at the level of $10 \mu\text{s}$ ([Reid & Honma, 2014](#)). By using this high precision technique, a handful of radio sources have been observed to measure their core shift (e.g., [Ros et al., 2001](#); [Martí-Vidal et al., 2011](#); [Rioja et al., 2015](#); [Dodson et al., 2017](#)). Moreover, it is shown that by applying a method of multi-frequency phase referencing, there is no need to observe any calibrator source and thus it can significantly reduce the observing time per source ([Dodson et al., 2017](#)). Both the self-referencing technique applied to our VGOS images and the phase referencing technique with external VLBI observations should be explored to determine the core shift of VGOS sources.

5 Conclusions

We have made images of extragalactic radio sources at the frequencies of 3.3 GHz, 5.5 GHz, 6.6 GHz, and 10.5 GHz based only on closure phases and closure amplitudes from broadband VGOS observations. A model fitting process equivalent to that used in producing broadband delay and δ TEC observables was applied to derive structure-induced delays and δ TEC, which were used to obtain modeled closures. These closures were compared with the observed ones. Structure effects in VGOS observations and the jumps in delays and δ TEC

observables were investigated in details. We finally discussed the impacts of reference points in the images at the four bands and core shift.

We tested the fidelity of our image reconstruction method by using simulated data with a known ground truth model and a (u, v) coverage and thermal noise properties identical to the actual VGOS observations. Closure-only imaging was demonstrated to be robust, and it produced consistent images for the sources with observations of more than 12 scans. So far with about 1100 scans and 80 sources in one 24-hour VGOS session, on average each source can have more than 12 scans. The IVS VGOS Technical Committee¹⁵ is working on reducing the integration time of an observation to be 10 seconds from the 30 seconds used at present. The number of scans in a session is expected to be more than doubled. These changes are promising for deriving images for a large number of sources from the VGOS observations with a good quality and a long time series in the VGOS era.

The closure-only images from the actual VGOS data predict source structure effects in broadband delays and δTEC very well. For the cases of sources 0016+731 and 1030+415, the RMS closure delays were 24.9 ps and 50.2 ps in session VO0034, respectively; the RMS residuals were 5.5 ps and 10.1 ps by correcting source structure effects. It was demonstrated that structure effects in broadband delays were dominated by source structure at higher frequencies, while those at the lowest frequency band were suppressed. The systematic errors in δTEC observables as shown in closure δTEC were also explained by these effects. Our study revealed that the jumps in delay and δTEC observables were caused by 2π phase shifts among the four bands due to strong source structure effects. They can be eventually resolved when the structure effects are taken into account. A big improvement in geodetic VLBI solution is expected by correcting these effects, and the study on this topic is in progress.

The absolute source position and the total flux are completely missed in the closure-only images. The main difficulty in correcting source structure effects is to identify the reference points in the images at the four bands in order to maintain stable source positions over time. External δTEC estimates with high accuracy may help to verify the reference points in the images and even determine core shift effects. The technique of self-referencing applied to VGOS images and external VLBI phase referencing measurements can also play an important role to determine these effects.

Based on this study, we argue that it is critical for VGOS observations to take source structure effects into account already in the post-correlation process and the observation scheduling, in order to minimize the random and systematic error contributions from these effects.

Acknowledgments

This research has made use of data from the MOJAVE database that is maintained by the MOJAVE team (Lister et al., 2018). This research was supported by the Academy of Finland project No. 315721.

References

- Akiyama, K., Kuramochi, K., Ikeda, S., Fish, V. L., Tazaki, F., Honma, M., ... Zaizen, M. (2017). Imaging the Schwarzschild-radius-scale Structure of M87 with the Event Horizon Telescope Using Sparse Modeling. *The Astrophysical Journal*, 838(1), 1. doi: 10.3847/1538-4357/aa6305
- Altamimi, Z., Rebischung, P., Métivier, L., & Collilieux, X. (2016). ITRF2014: A new release of the International Terrestrial Reference Frame modeling nonlinear sta-

¹⁵ <https://ivscc.gsfc.nasa.gov/about/com/vtc/index.html>

- tion motions. *Journal of Geophysical Research (Solid Earth)*, 121(8), 6109-6131. doi: 10.1002/2016JB013098
- Anderson, J. M., & Xu, M. H. (2018). Source Structure and Measurement Noise Are as Important as All Other Residual Sources in Geodetic VLBI Combined. *Journal of Geophysical Research (Solid Earth)*, 123(11), 10,162-10,190. doi: 10.1029/2018JB015550
- Blackburn, L., Pesce, D. W., Johnson, M. D., Wielgus, M., Chael, A. A., Christian, P., & Doeleman, S. S. (2020). Closure Statistics in Interferometric Data. *The Astrophysical Journal*, 894(1), 31. doi: 10.3847/1538-4357/ab8469
- Blandford, R. D., & Königl, A. (1979). Relativistic jets as compact radio sources. *The Astrophysical Journal*, 232, 34-48. doi: 10.1086/157262
- Bolotin, S., Baver, K., Bolotina, O., Gipson, J., Gordon, D., Le Bail, K., & MacMillan, D. (2019). The Source Structure Effect in Broadband Observations. In R. Haas, S. Garcia-Espada, & J. A. López Fernández (Eds.), *Proceedings of the 24th european VLBI group for geodesy and astrometry working meeting* (p. 224-228).
- Byrd, R. H., Lu, P., Nocedal, J., & Zhu, C. (1995). A limited memory algorithm for bound constrained optimization. *SIAM Journal on Scientific Computing*, 16(5), 1190-1208. Retrieved from <https://doi.org/10.1137/0916069> doi: 10.1137/0916069
- Cappallo, R. (2014). Correlating and Fringe-fitting Broadband VGOS Data. In *International VLBI service for geodesy and astrometry 2014 general meeting proceedings: "VGOS: The new VLBI network* (p. 91-96). Retrieved from https://ivsc.gsfc.nasa.gov/publications/gm2014/019_Cappallo.pdf
- Cappallo, R. (2015). Covariance Analysis of the Simultaneous Fit of Group Delay and dTEC in fourfit. In *Documentation of HOPS* (p. 1-5). Retrieved from https://www.haystack.mit.edu/tech/vlbi/hops/simulation_fit.pdf
- Cappallo, R. (2016). Delay and Phase Calibration in VGOS Post-Processing. In *New horizons with VGOS* (p. 61-64). Retrieved from https://ivsc.gsfc.nasa.gov/publications/gm2016/010_cappallo.pdf
- Chael, A. A., Johnson, M. D., Bouman, K. L., Blackburn, L. L., Akiyama, K., & Narayan, R. (2018). Interferometric Imaging Directly with Closure Phases and Closure Amplitudes. *The Astrophysical Journal*, 857(1), 23. doi: 10.3847/1538-4357/aab6a8
- Chael, A. A., Johnson, M. D., Narayan, R., Doeleman, S. S., Wardle, J. F. C., & Bouman, K. L. (2016). High-resolution Linear Polarimetric Imaging for the Event Horizon Telescope. *The Astrophysical Journal*, 829(1), 11. doi: 10.3847/0004-637X/829/1/11
- Clark, B. G. (1980). An efficient implementation of the algorithm 'CLEAN'. *Astronomy and Astrophysics*, 89(3), 377.
- Cornwell, T. J., & Wilkinson, P. N. (1981). A new method for making maps with unstable radio interferometers. *Monthly Notices of the Royal Astronomical Society*, 196, 1067-1086. doi: 10.1093/mnras/196.4.1067
- Dodson, R., Rioja, M. J., Molina, S. N., & Gómez, J. L. (2017). High-precision Astrometric Millimeter Very Long Baseline Interferometry Using a New Method for Multi-frequency Calibration. *The Astrophysical Journal*, 834(2), 177. doi: 10.3847/1538-4357/834/2/177
- Event Horizon Telescope Collaboration, Akiyama, K., Alberdi, A., Alef, W., Asada, K., Azulay, R., ... Yamaguchi, P. (2019). First M87 Event Horizon Telescope Results. IV. Imaging the Central Supermassive Black Hole. *The Astrophysical Journal Letters*, 875(1), L4. doi: 10.3847/2041-8213/ab0e85
- Fey, A. L., Gordon, D., Jacobs, C. S., Ma, C., Gaume, R. A., Arias, E. F., ... Zharov, V. (2015). The Second Realization of the International Celestial Reference Frame by Very Long Baseline Interferometry. *Astronomical Journal*, 150(2), 58. doi: 10.1088/0004-6256/150/2/58
- Hamaker, J. P., Bregman, J. D., & Sault, R. J. (1996). Understanding radio polarimetry. I. Mathematical foundations. *Astronomy and Astrophysics, Supplement*, 117, 137-147.
- Högbom, J. A. (1974). Aperture Synthesis with a Non-Regular Distribution of Interferometer Baselines. *Astronomy and Astrophysics Supplement*, 15, 417.
- Kovalev, Y. Y., Lobanov, A. P., Pushkarev, A. B., & Zensus, J. A. (2008). Opacity

- in compact extragalactic radio sources and its effect on astrophysical and astrometric studies. *Astronomy & Astrophysics*, 483, 759. doi: 10.1051/0004-6361/20078679
- Lister, M. L., Aller, M. F., Aller, H. D., Hodge, M. A., Homan, D. C., Kovalev, Y. Y., ... Savolainen, T. (2018). MOJAVE. XV. VLBA 15 GHz Total Intensity and Polarization Maps of 437 Parsec-scale AGN Jets from 1996 to 2017. *The Astrophysical Journal Supplement*, 234(1), 12. doi: 10.3847/1538-4365/aa9c44
- Martí-Vidal, I., Marcaide, J. M., Alberdi, A., Pérez-Torres, M. A., Ros, E., & Guirado, J. C. (2011). Detection of jet precession in the active nucleus of M 81. *Astronomy & Astrophysics*, 533, A111. doi: 10.1051/0004-6361/201117211
- Narayan, R., & Nityananda, R. (1986). Maximum entropy image restoration in astronomy. *Annual Review of Astron and Astrophys*, 24, 127-170. doi: 10.1146/annurev.aa.24.090186.001015
- Niell, A., Barrett, J., Burns, A., Cappallo, R., Corey, B., Derome, M., ... Petrachenko, B. (2018). Demonstration of a Broadband Very Long Baseline Interferometer System: A New Instrument for High-Precision Space Geodesy. *Radio Science*, 53(10), 1269-1291. doi: 10.1029/2018RS006617
- Niell, A., Whitney, A., Petrachenko, W., Schlüter, W., Vandenberg, N., Hase, H., ... Tuccari, G. (2007). VLBI2010: a Vision for Future Geodetic VLBI. In P. Tregoning & C. Rizos (Eds.), *Dynamic planet - monitoring and understanding a dynamic planet with geodetic and oceanographic tools, edited by paul tregoning and chris rizos. isbn isbn 978-3-540-49349-5. berlin: Springer, 2007., p.757 (p. 757)*. Retrieved from https://link.springer.com/chapter/10.1007/978-3-540-49350-1_108
- Nityananda, R., & Narayan, R. (1983). Reconstruction of a polarized brightness distribution by the maximum entropy method. *Astronomy and Astrophysics*, 118(1), 194-196.
- Nothnagel, A., Artz, T., Behrend, D., & Malkin, Z. (2017). International VLBI Service for Geodesy and Astrometry. Delivering high-quality products and embarking on observations of the next generation. *Journal of Geodesy*, 91(7), 711-721. doi: 10.1007/s00190-016-0950-5
- Pearson, T. J., & Readhead, A. C. S. (1984). Image Formation by Self-Calibration in Radio Astronomy. *Annual Review of Astron and Astrophys*, 22, 97-130. doi: 10.1146/annurev.aa.22.090184.000525
- Petrachenko, B., Niell, A., Behrend, D., Corey, B., Boehm, J., Charlot, P., ... Wresnik, J. (2009). *Design Aspects of the VLBI2010 System. Progress Report of the IVS VLBI2010 Committee, June 2009*. (Tech. Rep.). Retrieved from <https://ivscc.gsfc.nasa.gov/publications/misc/TM-2009-214180.pdf>
- Plavin, A. V., Kovalev, Y. Y., Pushkarev, A. B., & Lobanov, A. P. (2019). Significant core shift variability in parsec-scale jets of active galactic nuclei. *Monthly Notices of the Royal Astronomical Society*, 485(2), 1822-1842. doi: 10.1093/mnras/stz504
- Porcas, R. W. (2009). Radio astrometry with chromatic AGN core positions. *Astronomy & Astrophysics*, 505(1), L1-L4. doi: 10.1051/0004-6361/200912846
- Porcas, R. W. (2010). VLBI2010: The Astro-Geo Connection. In R. Navarro et al. (Eds.), *Sixth international VLBI service for geodesy and astronomy. Proceedings from the 2010 general meeting (p. 8-17)*. Retrieved from <https://ivscc.gsfc.nasa.gov/publications/gm2010/porcas.pdf>
- Pushkarev, A. B., Hovatta, T., Kovalev, Y. Y., Lister, M. L., Lobanov, A. P., Savolainen, T., & Zensus, J. A. (2012). MOJAVE: Monitoring of Jets in Active galactic nuclei with VLBA Experiments. IX. Nuclear opacity. *Astronomy & Astrophysics*, 545, A113. doi: 10.1051/0004-6361/201219173
- Reid, M. J., & Honma, M. (2014). Microarcsecond Radio Astrometry. *Annual Review of Astronomy and Astrophysics*, 52, 339-372. doi: 10.1146/annurev-astro-081913-040006
- Rioja, M. J., Dodson, R., Jung, T., & Sohn, B. W. (2015). The Power of Simultaneous Multifrequency Observations for mm-VLBI: Astrometry up to 130 GHz with the KVN. *Astronomical Journal*, 150(6), 202. doi: 10.1088/0004-6256/150/6/202
- Ros, E., Marcaide, J. M., Guirado, J. C., & Pérez-Torres, M. A. (2001). Absolute kinematics

- of radio source components in the complete S5 polar cap sample. I. First and second epoch maps at 8.4 GHz. *Astronomy & Astrophysics*, 376, 1090-1105. doi: 10.1051/0004-6361:20010987
- Schuh, H., & Behrend, D. (2012). VLBI: A fascinating technique for geodesy and astrometry. *Journal of Geodynamics*, 61, 68-80. doi: 10.1016/j.jog.2012.07.007
- Sokolovsky, K. V., Kovalev, Y. Y., Pushkarev, A. B., & Lobanov, A. P. (2011). A VLBA survey of the core shift effect in AGN jets. I. Evidence of dominating synchrotron opacity. *Astronomy & Astrophysics*, 532, A38. doi: 10.1051/0004-6361/201016072
- Thompson, A. R., Moran, J. M., & Swenson, J., George W. (2017). *Interferometry and Synthesis in Radio Astronomy, 3rd Edition*. doi: 10.1007/978-3-319-44431-4
- Wilkinson, P. N., Readhead, A. C. S., Purcell, G. H., & Anderson, B. (1977). Radio structure of 3C 147 determined by multi-element very long baseline interferometry. *Nature*, 269, 764-768. doi: 10.1038/269764a0
- Xu, M. H., Anderson, J. M., Heinkelmann, R., Lunz, S., Schuh, H., & Wang, G. L. (2019). Structure Effects for 3417 Celestial Reference Frame Radio Sources. *The Astrophysical Journal Supplement Series*, 242(1), 5. doi: 10.3847/1538-4365/ab16ea
- Xu, M. H., Anderson, J. M., Heinkelmann, R., Lunz, S., Schuh, H., & Wang, G. L. (2020). Observable quality assessment of broadband very long baseline interferometry system. *Submitted to Journal of Geodesy*. doi: Notavailable
- Xu, M. H., Heinkelmann, R., Anderson, J. M., Mora-Diaz, J., Karbon, M., Schuh, H., & Wang, G. L. (2017). The impacts of source structure on geodetic parameters demonstrated by the radio source 3C371. *Journal of Geodesy*, 91(7), 767-781. doi: 10.1007/s00190-016-0990-x
- Xu, M. H., Heinkelmann, R., Anderson, J. M., Mora-Diaz, J., Schuh, H., & Wang, G. L. (2016). The Source Structure of 0642+449 Detected from the CONT14 Observations. *Astronomical Journal*, 152(5), 151. doi: 10.3847/0004-6256/152/5/151

6 Appendix

6.1 Models of source structure effects

Consider that a source has an image at the frequency of ν with N components and the flux of the i -th component is A_i . An arbitrary point in the image, O , is selected as the reference to describe the relative position of the i -th component, $\Delta\vec{k}_i$. Phase due to structure effect of this source on a baseline with the (u, v) vector of \vec{b} is written as

$$\phi_\nu^{\text{str}} = \tan^{-1} \frac{\sum_{i=1}^N A_i \cos(2\pi\nu\vec{k}_i \cdot \vec{b}/c)}{\sum_{i=1}^N A_i \sin(2\pi\nu\vec{k}_i \cdot \vec{b}/c)}, \quad (9)$$

where c is the speed of light.

The delay due to source structure can be given by

$$\tau_\nu^{\text{str}} = \frac{\partial\phi_\nu^{\text{str}}}{\partial\nu}. \quad (10)$$

Notice that this equation can be applicable, for instance, for group delays at S or X band, but not for broadband delays.

Observed amplitude, V_ν^{str} is given as follows

$$V_\nu^{\text{str}} = \sqrt{\left[\sum_{i=1}^N A_i \cos(2\pi\nu\vec{k}_i \cdot \vec{b}/c)\right]^2 + \left[\sum_{i=1}^N A_i \sin(2\pi\nu\vec{k}_i \cdot \vec{b}/c)\right]^2}. \quad (11)$$

6.2 Closure phases of source 0016+731

In total, source 0016+731 has 1879 closure phases in session VO0034 with root-mean-square (RMS) values of 4.5° at 3.3 GHz, 9.7° at 5.5 GHz, 17.3° at 6.6 GHz, and 30.4° at 10.5 GHz. By subtracting the modeled closure phases from the observed ones, the RMS values of the residuals are 4.4° , 4.1° , 4.8° , and 6.5° at the four bands, respectively. Figure 13 shows the closure phases of triangle GGA012M–ISHIOKA–WETTZ13S from actual observations in blue dots and from the derived images in green open circles. The error bars of observed closure phases are calculated from the derived uncertainties of phases on the three baselines of each individual closure.

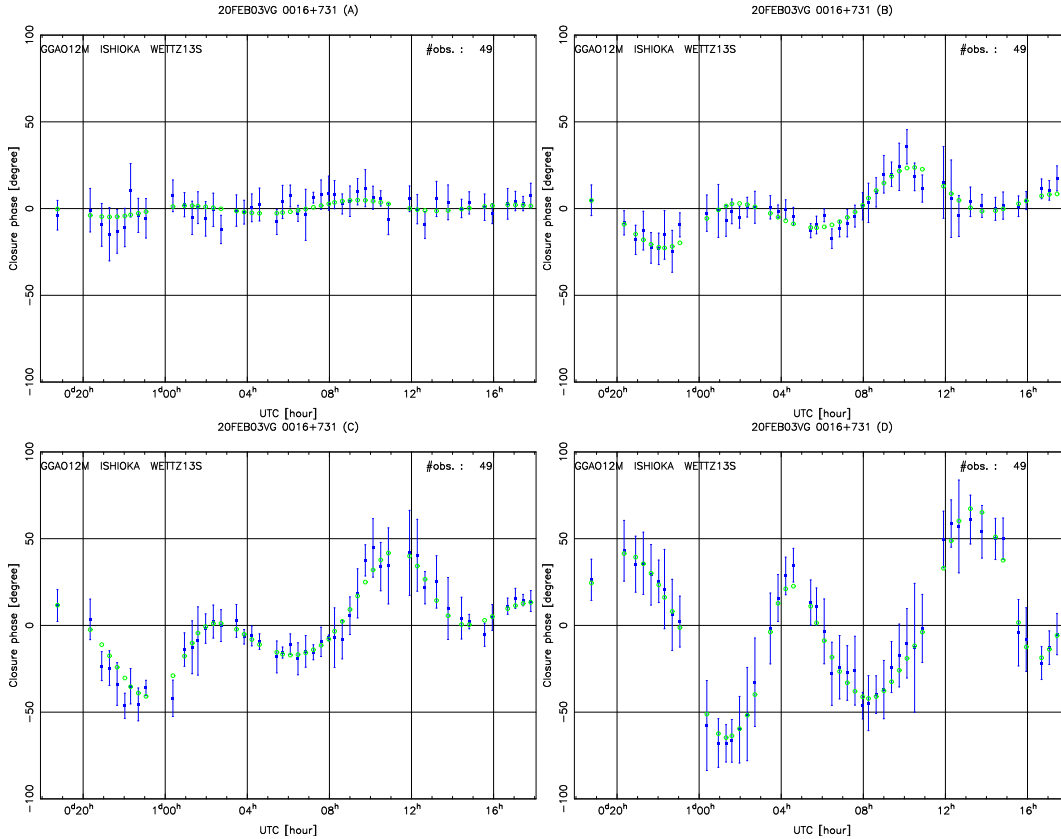


Figure 13. Observed closure phases (blue dots) and modeled closure phases (green open circles) of triangle GGA012M–ISHIOKA–WETTZ13S for source 0016+731 at the frequencies 3.3 GHz (upper-left), 5.5 GHz (upper-right), 6.6 GHz (bottom-left), and 10.5 GHz (bottom-right) in session VO0034. The RMS values of the closure phases of this triangle are 6.5° , 12.5° , 22.5° , and 36.9° at the four bands; by subtracting the modeled closure phases, the RMS values of the residual closure phases are 5.5° , 5.0° , 6.0° , and 6.2° .

6.3 Images for some representative sources

The images for the other seven sources, based on which structure effects have been discussed in the main body of the paper, are presented in Figures 14, 17, 18, 19, 20, 21, and 22. Comparison plots for closure phases and log closure amplitudes are shown only for source 1803+784 in Figures 15 and 16 as an example.

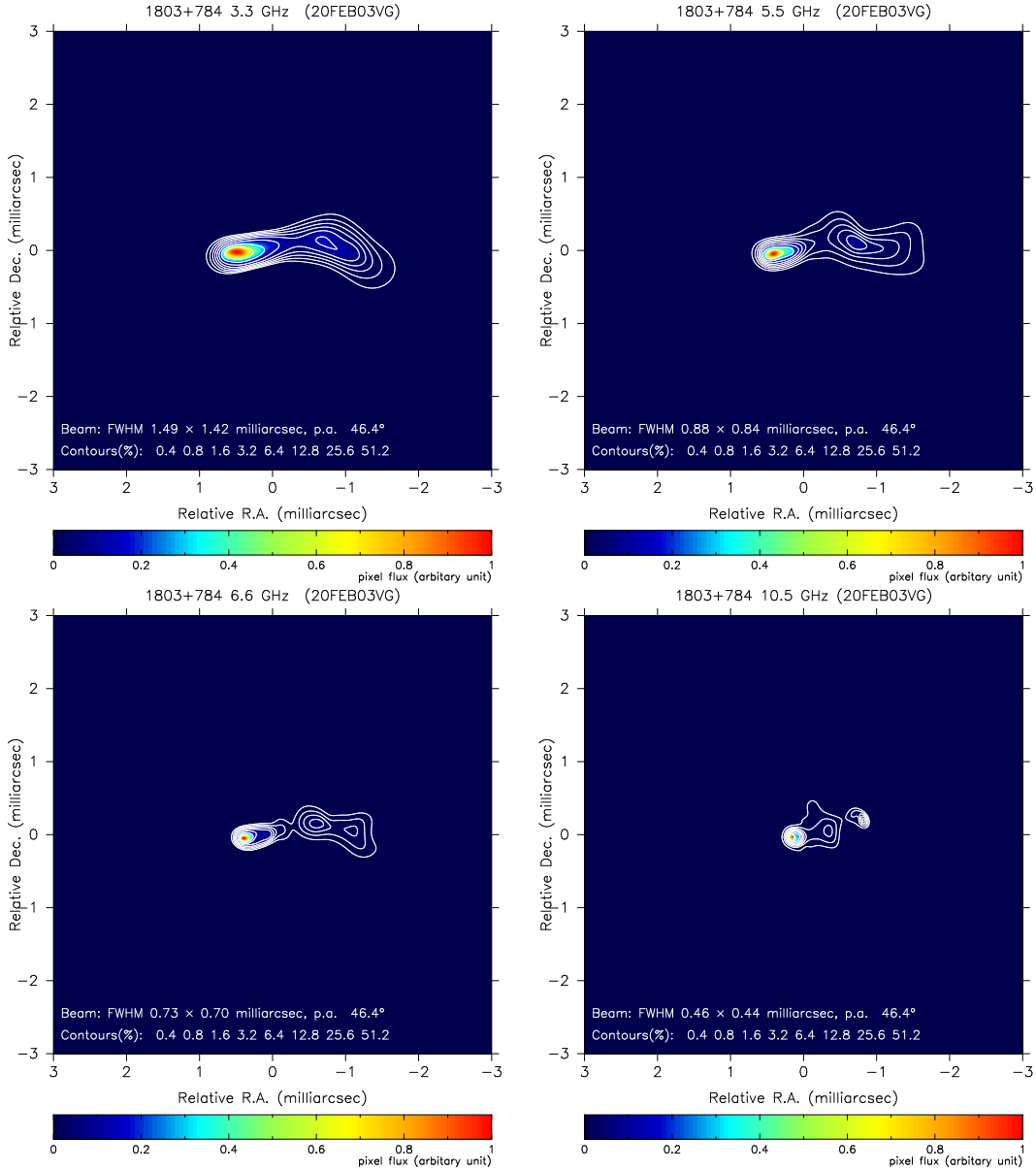


Figure 14. Images of source 1803+784 at the frequencies of 3.3 GHz, 5.5 GHz, 6.6 GHz, and 10.5 GHz from VGOS observations VO0034. Overlay contours are shown at eight levels of peak percentage (specified in the bottom of plots) in white. They were derived based on closure phases and closure amplitudes only. The mean flux positions are chosen as the reference points for the plots and the pixel fluxes are in arbitrary units. The coordinates of the maximum flux points are (0.487, -0.030), (0.412, -0.048), (0.389, -0.055), and (0.144, -0.039) mas for the four bands, respectively. The beam parameters are shown in the bottom of each plot.

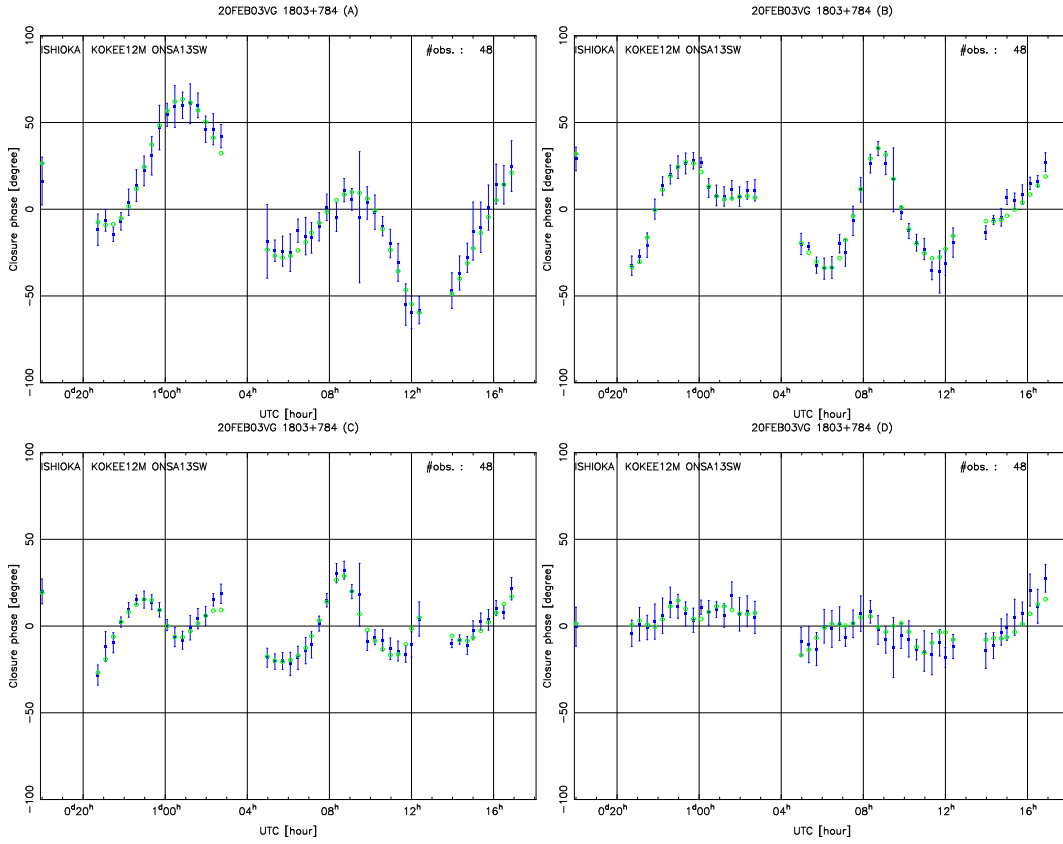


Figure 15. Observed closure phases (blue dots) and modeled closure phases (green open circles) of triangle ISHIOKA–KOKEE12M–ONSA13SW for source 1803+784 at the frequencies 3.3 GHz (upper-left), 5.5 GHz (upper-right), 6.6 GHz (bottom-left), and 10.5 GHz (bottom-right) in session VO0034.

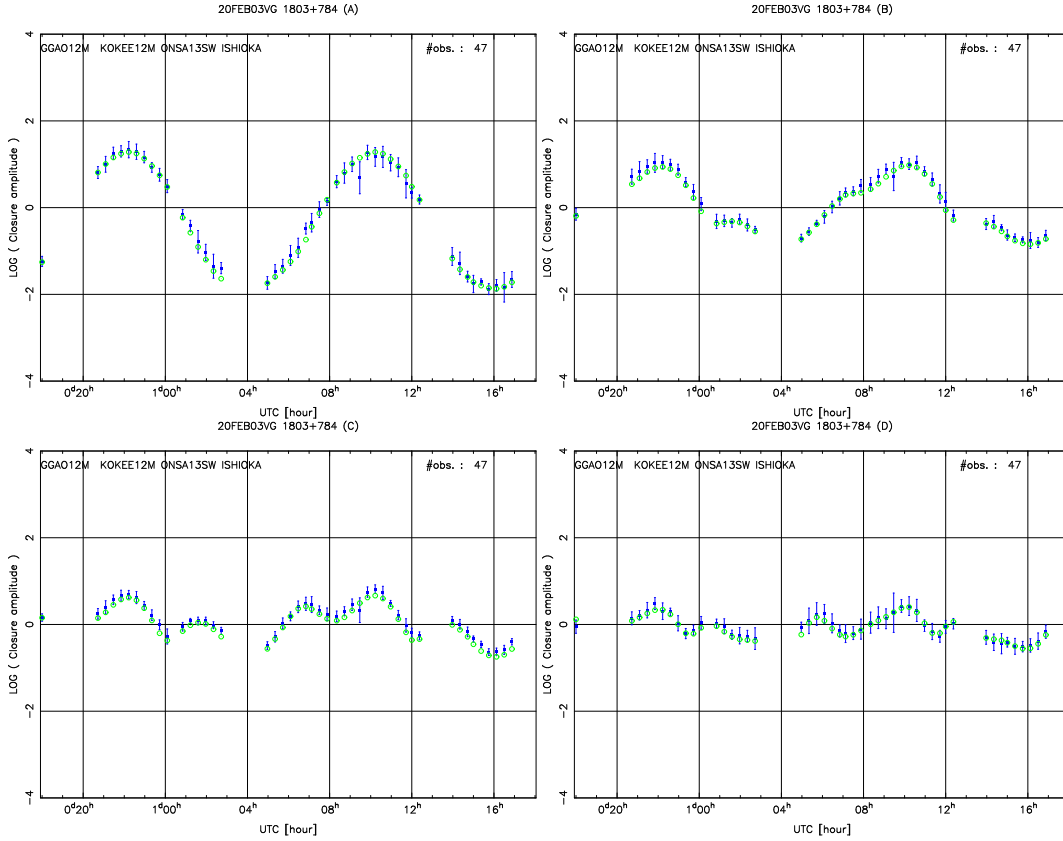


Figure 16. Observed log closure amplitudes (blue dots) and modeled log closure amplitudes (green open circles) of quadrangle GGAO12M–KOKEE12M–ONSA13SW–ISHIOKA for source 1803+784 at the frequencies 3.3 GHz (upper-left), 5.5 GHz (upper-right), 6.6 GHz (bottom-left), and 10.5 GHz (bottom-right) in session VO0034.

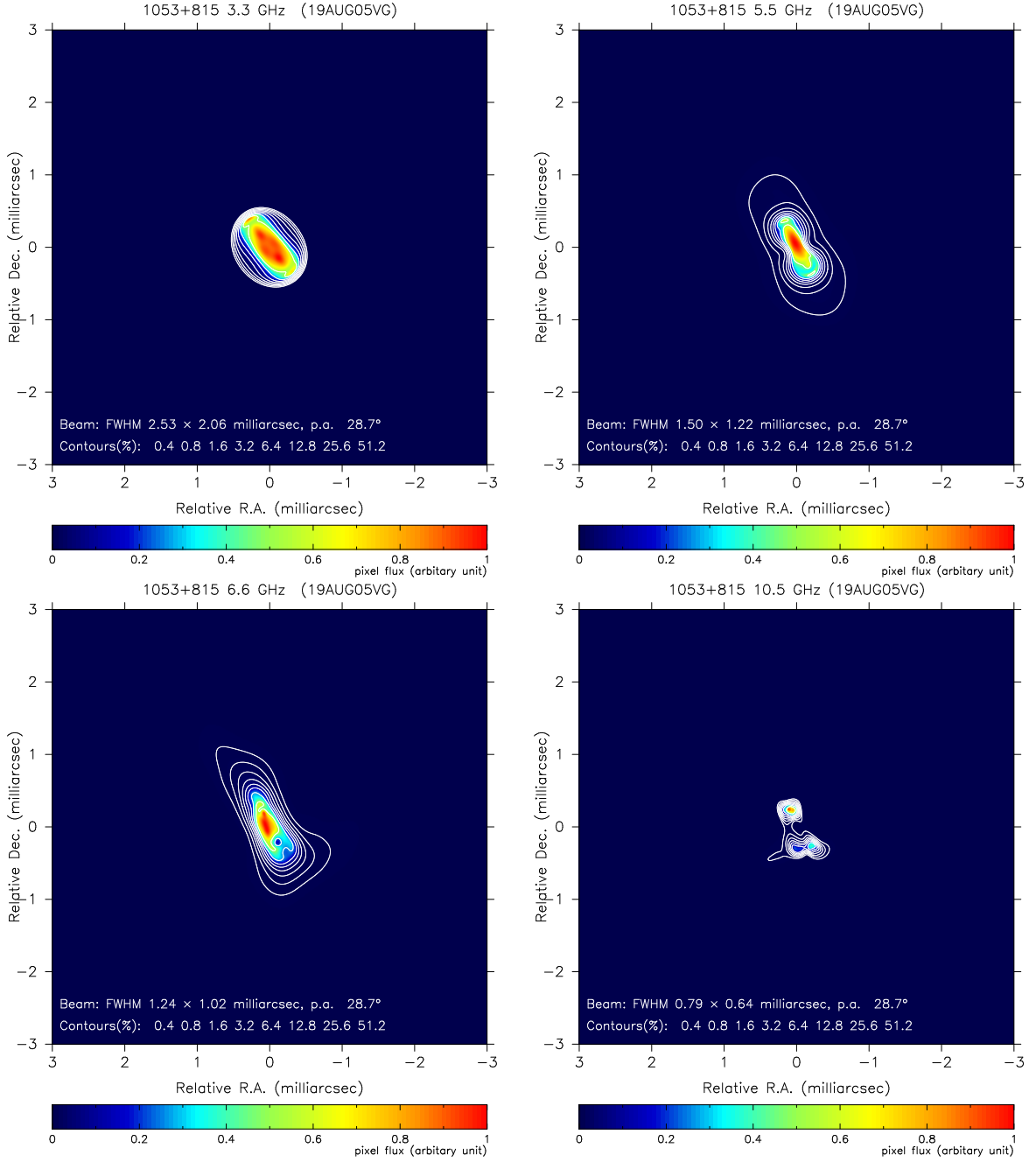


Figure 17. Images of source 1053+815 at the frequencies of 3.3 GHz, 5.5 GHz, 6.6 GHz, and 10.5 GHz from VGOS observations VT9217. Overlay contours are shown at eight levels of peak percentage (specified in the bottom of plots) in white. They were derived based on closure phases and closure amplitudes only. The mean flux positions are chosen as the reference points for the plots and the pixel fluxes are in arbitrary units. The coordinates of the maximum flux points are $(-0.120, -0.144)$, $(0.023, 0.047)$, $(0.050, -0.004)$, and $(0.113, -0.238)$ mas for the four bands, respectively. The beam parameters are shown in the bottom of each plot.

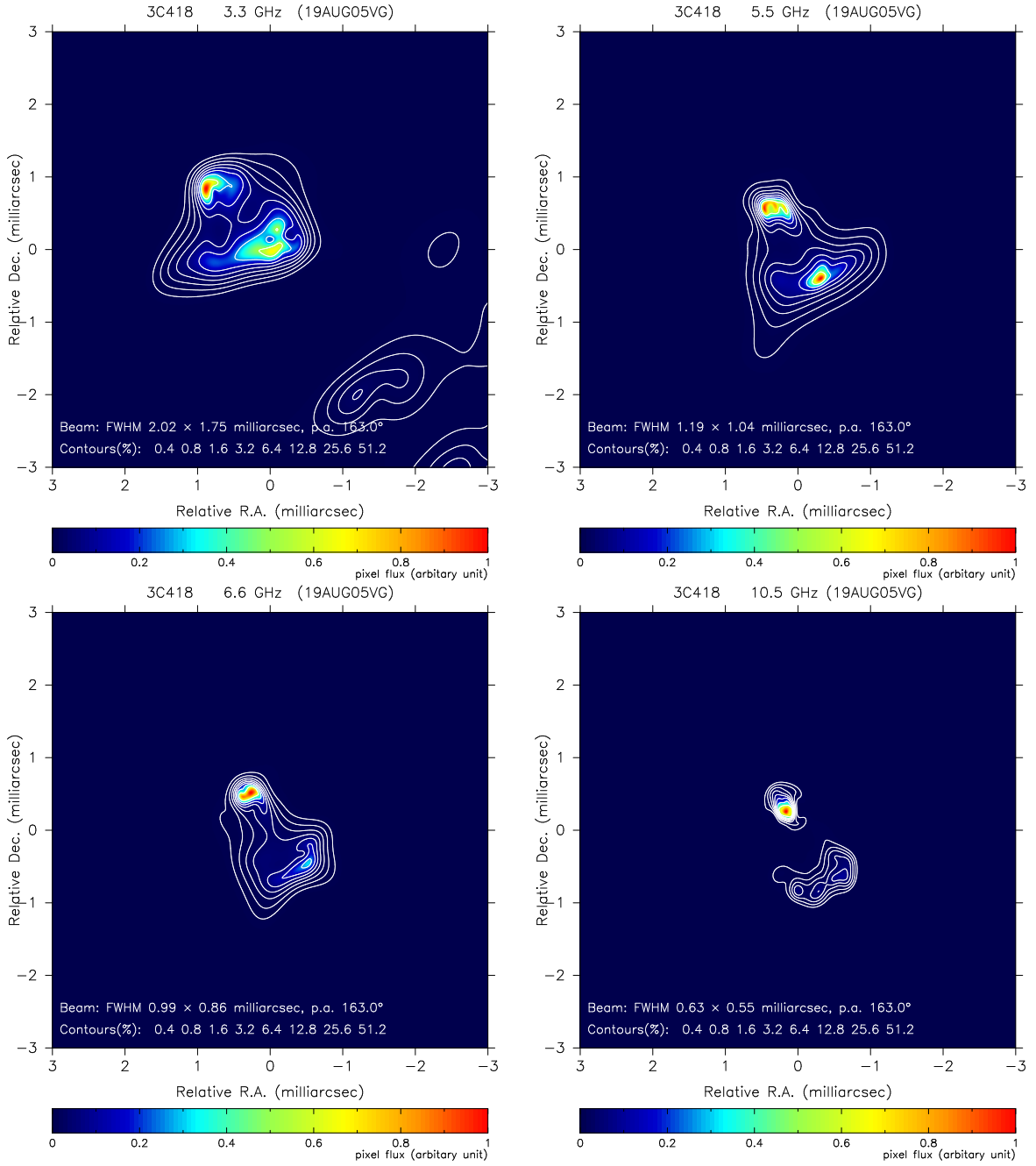


Figure 18. Images of source 3C418 at the frequencies of 3.3 GHz, 5.5 GHz, 6.6 GHz, and 10.5 GHz from VGOS observations VT9217. Overlay contours are shown at eight levels of peak percentage (specified in the bottom of plots) in white. They were derived based on closure phases and closure amplitudes only. The mean flux positions are chosen as the reference points for the plots and the pixel fluxes are in arbitrary units. The coordinates of the maximum flux points are (0.890, 0.832), (−0.303, −0.404), (0.268, 0.515), and (0.165, −0.253) mas for the four bands, respectively. The beam parameters are shown in the bottom of each plot.

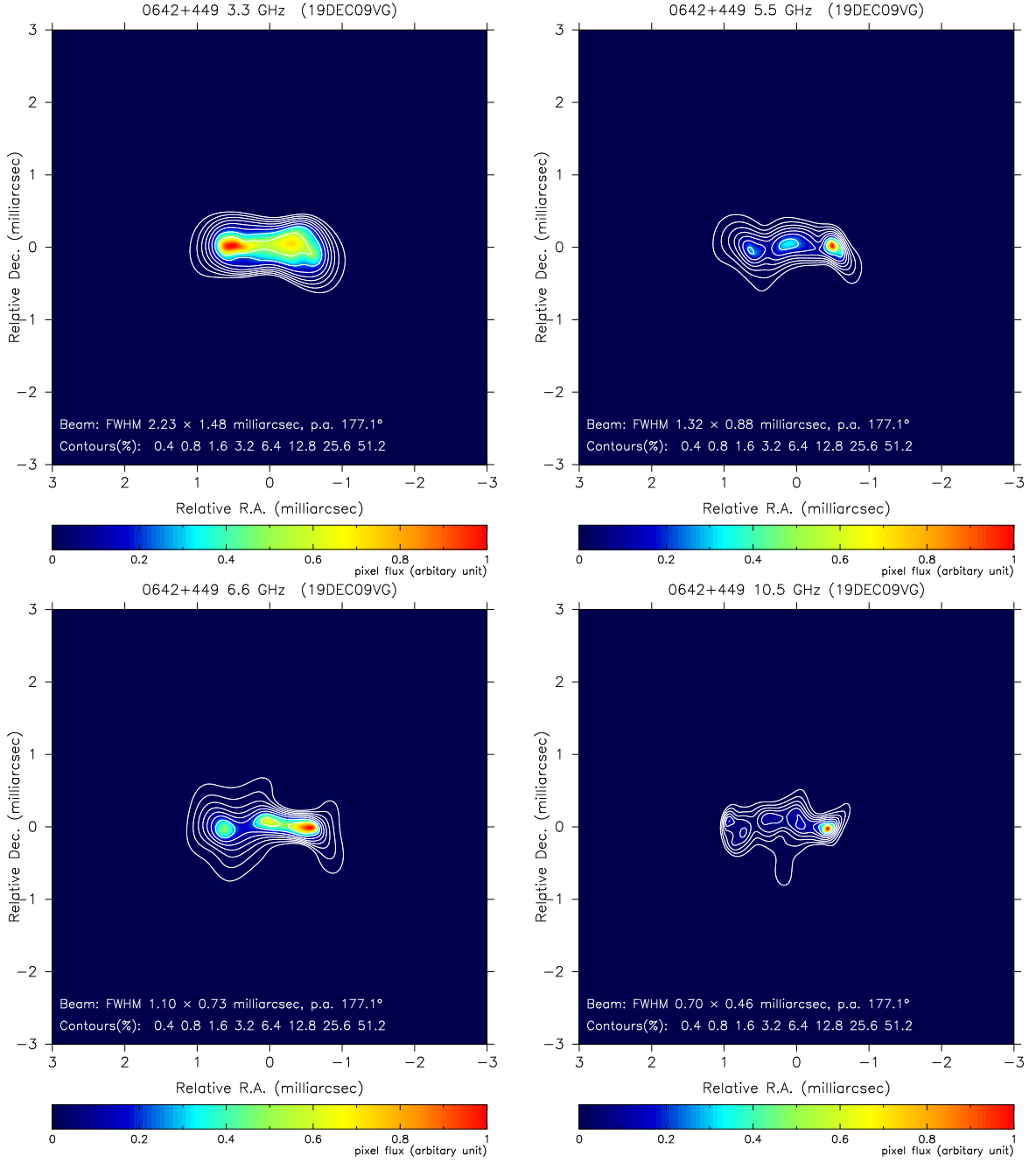


Figure 19. Images of source 0642+449 at the frequencies of 3.3 GHz, 5.5 GHz, 6.6 GHz, and 10.5 GHz from VGOS observations VT9343. Overlay contours are shown at eight levels of peak percentage (specified in the bottom of plots) in white. They were derived based on closure phases and closure amplitudes only. The mean flux positions are chosen as the reference points for the plots and the pixel fluxes are in arbitrary units. The coordinates of the maximum flux points are (0.544, 0.006), (−0.486, 0.015), (−0.561, −0.014), and (−0.424, −0.033) mas for the four bands, respectively. The beam parameters are shown in the bottom of each plot.

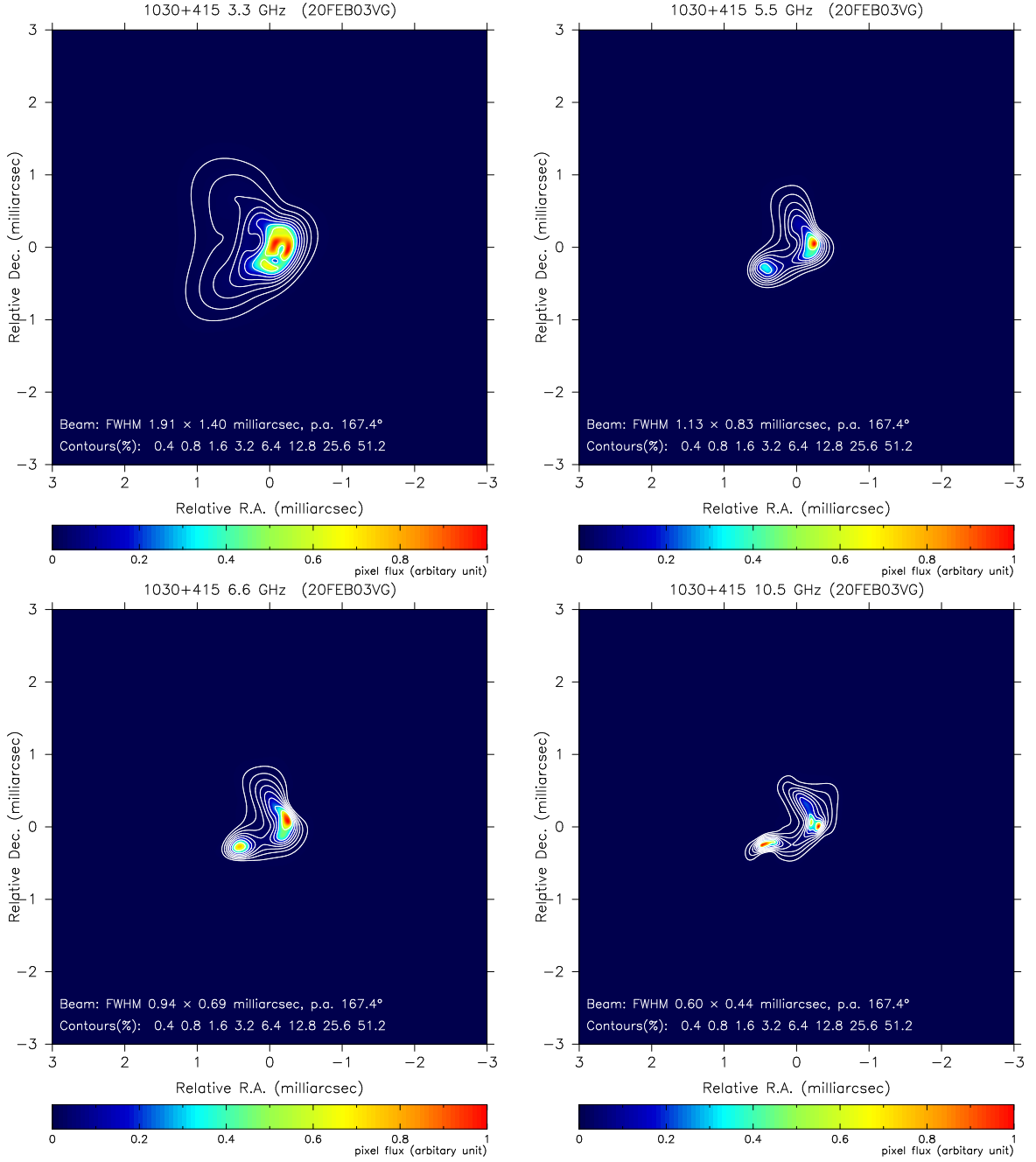


Figure 20. Images of source 1030+415 at the frequencies of 3.3 GHz, 5.5 GHz, 6.6 GHz, and 10.5 GHz from VGOS observations VO0034. Overlay contours are shown at eight levels of peak percentage (specified in the bottom of plots) in white. They were derived based on closure phases and closure amplitudes only. The mean flux positions are chosen as the reference points for the plots and the pixel fluxes are in arbitrary units. The coordinates of the maximum flux points are $(-0.252, -0.046)$, $(-0.230, 0.041)$, $(-0.245, 0.082)$, and $(-0.308, 0.056)$ mas for the four bands, respectively. The beam parameters are shown in the bottom of each plot.

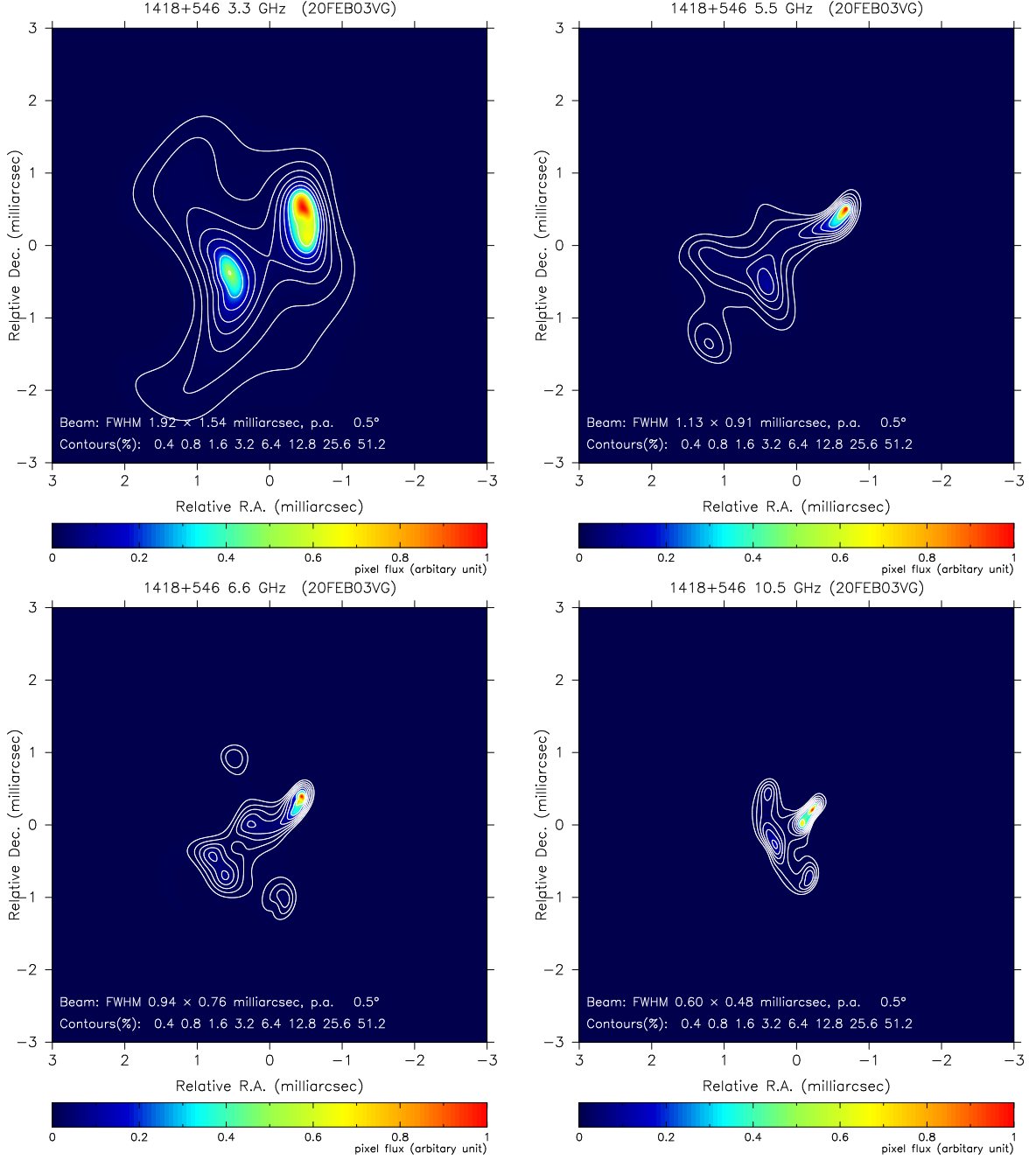


Figure 21. Images of source 1418+546 at the frequencies of 3.3 GHz, 5.5 GHz, 6.6 GHz and 10.5 GHz from VGOS observations VO0034. Overlay contours are shown at eight levels of peak percentage (specified in the bottom of plots) in white. They were derived based on closure phases and closure amplitudes only. The mean flux positions are chosen as the reference points for the plots and the pixel fluxes are in arbitrary units. The coordinates of the maximum flux points are $(-0.458, 0.520)$, $(-0.672, 0.494)$, $(-0.439, 0.388)$, and $(-0.210, 0.199)$ mas for the four bands, respectively. The beam parameters are shown in the bottom of each plot.

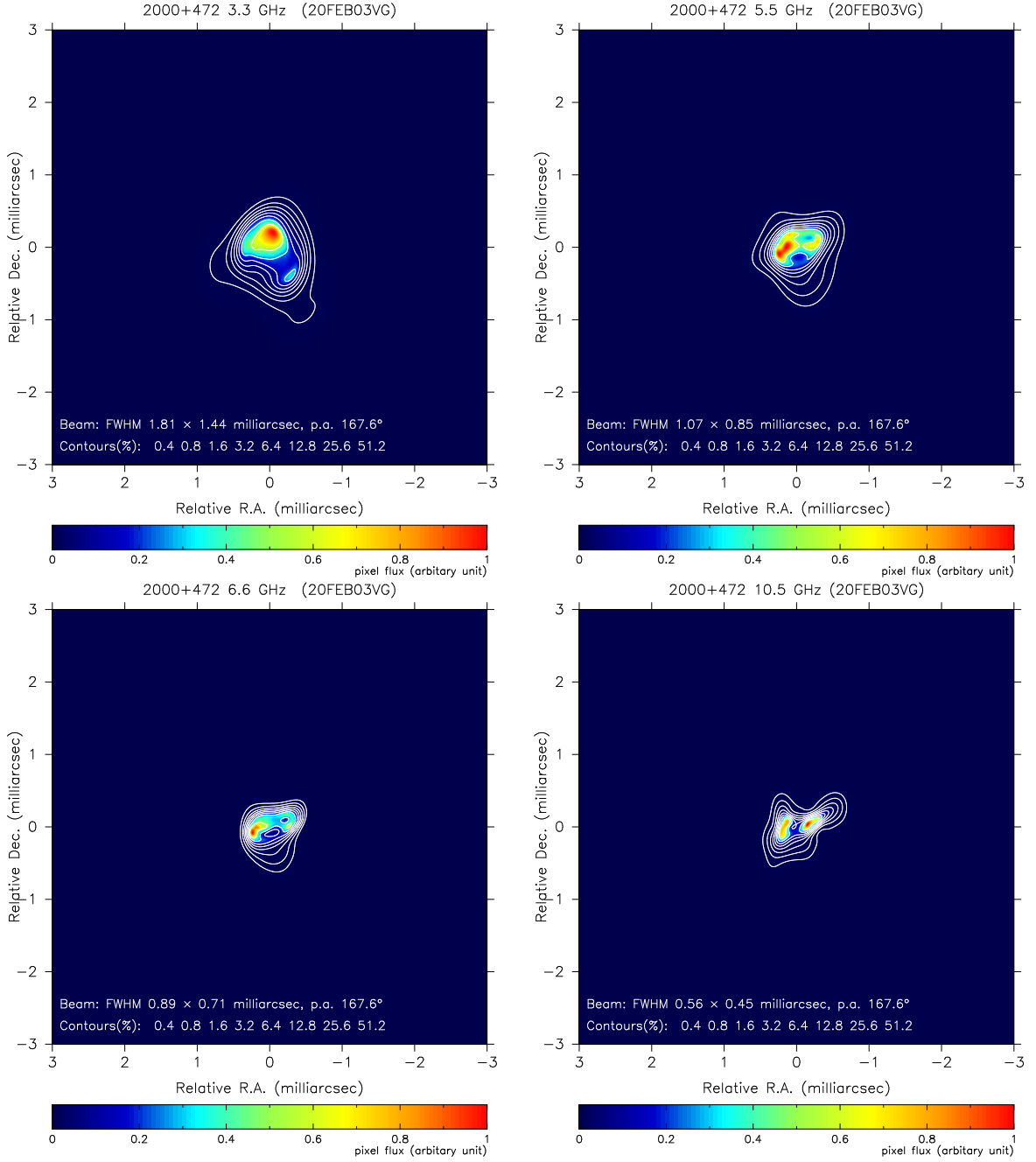


Figure 22. Images of source 2000+472 at the frequencies of 3.3 GHz, 5.5 GHz, 6.6 GHz, and 10.5 GHz from VGOS observations VO0034. Overlay contours are shown at eight levels of peak percentage (specified in the bottom of plots) in white. They were derived based on closure phases and closure amplitudes only. The mean flux positions are chosen as the reference points for the plots and the pixel fluxes are in arbitrary units. The coordinates of the maximum flux points are $(-0.042, 0.201)$, $(0.247, -0.100)$, $(0.232, -0.082)$, and $(-0.150, 0.031)$ mas for the four bands, respectively. The beam parameters are shown in the bottom of each plot.

6.4 MOJAVE images of six sources

The images of six sources from the MOJAVE project were used in the study for simulation and comparison.

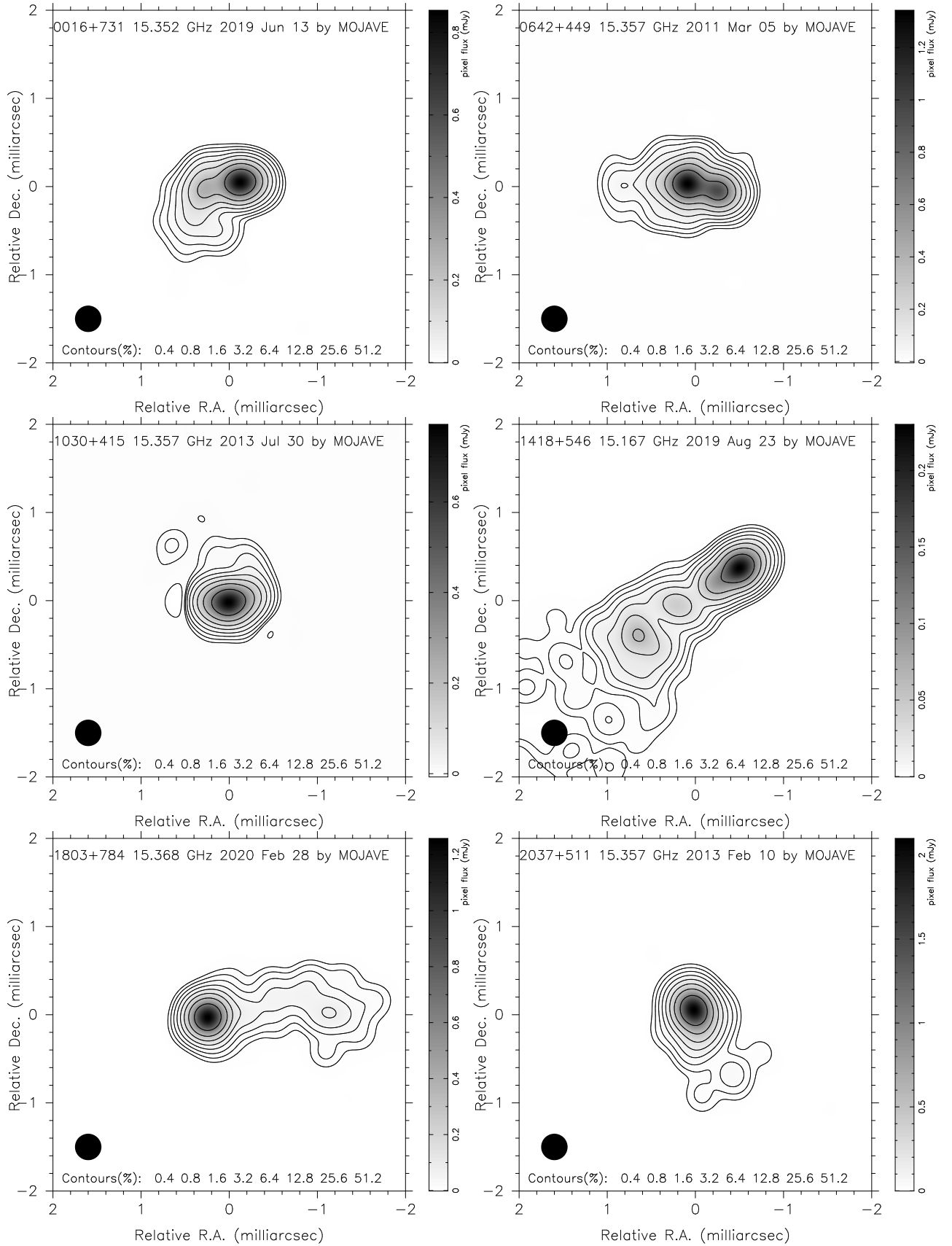


Figure 23. MOJAVE images of the 6 sources used for simulation and comparison at the epochs close to the VGOS observations. They were convolved with a circular beam of 0.3 mas, about 40% of the typical MOJAVE beam size.